Journal of the Energy Institute 111 (2023) 101404

Contents lists available at ScienceDirect

Journal of the Energy Institute

journal homepage: www.elsevier.com/locate/joei

Atomization and combustion behavior of nanofuel droplets containing perovskite-type nanoparticles

Rıdvan Küçükosman [a], Aleyna Akçay [b], Ahmet Alper Yontar [c,*], Cumhur Gökhan Ünlü [d], Kasim Ocakoglu [e]

[a] Department of Manufacturing Engineering, School of Graduate Studies, Tarsus University, Tarsus, Mersin, Turkey
[b] Department of Biomedical Engineering, Institute of Science, Pamukkale University, Denizli, Turkey
[c] Department of Mechanical Engineering, Faculty of Engineering, Tarsus University, Tarsus, Mersin, Turkey
[d] Department of Biomedical Engineering, Faculty of Technology, Pamukkale University, Denizli, Turkey
[e] Department of Engineering Fundamental Sciences, Faculty of Engineering, Tarsus University, Tarsus, Mersin, Turkey

ARTICLE INFO

Keywords:
Nanoparticles
Nanofuels
La-based perovskite-type oxides
Neodymium
Combustion catalysts

ABSTRACT

Metal and metal oxide nanoparticles (NPs) are promising agents for reducing energy consumption and pollution in applications where combustion power generation is provided. This study focuses on the production of new generation perovskite-type metal oxide NPs with enhanced catalytic activity customized for combustion and investigation of their catalytic performance for gasoline. The droplet scale combustion experiments were carried out at ambient temperature, atmospheric pressure and under normal gravity, the experimental processes were recorded with an optical system consisting of a high-speed camera and a thermal camera with a spectral range of 7.5–14 μm, and the combustion and atomization behavior of the nanofuel droplets were characterized. Perovskite-type NPs were produced by sol-gel technique in varying stoichiometric ratios ($LaMnO_3$, $La_{1-X}Nd_XMnO_3$, $La_{1-X}Ba_XMnO_3$, $Nd_{1-X}Ba_XMnO_3$, $La_{0.5}Nd_XBa_{0.5-X}MnO_3$, x = 0, 0.3) to confirm their catalytic activity's effect on gasoline droplets' combustion behavior. Structural characterization of the obtained five different NPs was carried out by SEM and XRD techniques. Chemical analysis, surface area measurements, and spectral properties of the samples were determined by XPS, BET, and UV–Vis spectroscopy, respectively. The results showed that all perovskite-type NPs have particle size range of 25–40 nm. $La_{0.7}Nd_{0.3}MnO_3$ NPs had the highest oxygen adsorption ability and $La_{0.5}Nd_{0.3}Ba_{0.2}MnO_3$ NPs had the largest surface area (393.4898 m^2/g). Perovskite type NPs tended to increase ignition delay and extinction times. The maximum flame temperature of fuel droplets loaded with $La_{0.5}Nd_{0.3}Ba_{0.2}MnO_3$ NPs was 469 °C. This temperature was 274 °C higher than the maximum flame temperature of the pure gasoline droplet. The outcomes demonstrated that, with the right catalyst design, perovskite-type NPs can perform better as powerful oxidizers and high energy combustion catalysts.

1. Introduction

Nanofuels are new generation fuels containing nano-sized functional agents that regulate the combustion, atomization, and emission behavior of the base fuel. Nanomaterials with improved physical properties can reduce the activation energy required for combustion reactions as a catalyst, facilitate hydrocarbon oxidation, and increase the volumetric and mass-energy density of the fuel depending on the calorific value of the components [1]. In addition, they can provide rich air-fuel mixtures by improving the atomization mechanism in liquid fuels [2]. NP additives, which function as combustion regulating and improving agents (Al, Fe, B, MgO, Fe_2O_3, Al_2O_3, etc.) [3], can be produced by various methods such as solid-phase reactions [4], wet chemical synthesis [5], chemical precipitation [6], chemical vapor deposited (CVD) [7], hydrothermal reaction [8], sol-gel [9].

The ability to produce materials with targeted properties at the nanoscale, combined with recent advances in nanotechnology, has led to the discovery of a new class of high energy density fuels containing high energy density NP catalysts [10]. It is well known that the enhanced catalytic activity results from synergistic effects mediated by the materials' lattice structure defect (void), surface oxygen mobility, and the reduction-oxidation (redox) properties of catalysts. Perovskite-type NPs are among the most advanced materials of this class, with their low

* Corresponding author.
E-mail address: aayontar@tarsus.edu.tr (A.A. Yontar).

https://doi.org/10.1016/j.joei.2023.101404
Received 19 April 2023; Received in revised form 10 September 2023; Accepted 21 September 2023
Available online 22 September 2023
1743-9671/© 2023 Energy Institute. Published by Elsevier Ltd. All rights reserved.

Nomenclature

BET	Brunauer–Emmett–Teller theory
CVD	Chemical Vapor Deposition
GA	Gasoline
GA + OA	Gasoline + oleic acid
GA + LM1	Gasoline + $LaMnO_3$
GA + LNM1	Gasoline + $La_{0.7}Nd_{0.3}MnO_3$
GA + NBM	Gasoline + $Nd_{0.7}Ba_{0.3}MnO_3$
GA + LBM	Gasoline + $La_{0.7}Ba_{0.3}MnO_3$
GA + LNBM1	Gasoline + $La_{0.5}Nd_{0.3}Ba_{0.2}MnO_3$
ID	Ignition Delay
LM1	$LaMnO_3$
LNM1	$La_{0.7}Nd_{0.3}MnO_3$
NBM	$Nd_{0.7}Ba_{0.3}MnO_3$
LBM	$La_{0.7}Ba_{0.3}MnO_3$
LNBM1	$La_{0.5}Nd_{0.3}Ba_{0.2}MnO_3$
NP	Nanoparticle
OA	Oleic acid
SEM	Scanning electron microscope
XRD	X-Ray diffraction spectroscopy
XPS	X-ray photoelectron spectroscopy
UV–Vis	Ultraviolet and visible (UV–Vis) absorption spectroscopy

activation energies, active edges, large surface areas, high oxygen absorption capabilities, diversification in their components, easy production in stoichiometric and non-stoichiometric ratios, and cheapness [11]. However, the fabrication techniques used for the utilization of perovskite NPs alter properties such as particle size, surface area, morphology, crystal shape, surface composition and distribution. One of the best methods for producing perovskite-type metal oxide NPs with a uniform particle size distribution in the precipitate phase is the sol-gel method [12].

Perovskite-type oxides with the general formula ABO_3, where A = lanthanide element and B = transition metal, show significant catalytic activity in many reactions [13]. $LaFeO_3$, $LaCoO_3$, $LaMnO_3$, LaOCl, $La_{0.8}Sr_{0.2}MnO_3$ NPs have long been preferred for reducing the thermal decomposition and combustion reaction temperatures of propellants such as RDX, HMX, and AP [10]. It is now stated that the molecular perovskite energetic material DAP-4 exhibits high energy property and strong oxidation ability for the ignition and combustion of boron, and thus molecular perovskite energetic materials have the potential to be a new candidate for potential application in high-energy B-based solid rocket propellants [14].

In recent years, perovskites have been used for the catalytic combustion of highly volatile compounds such as methane, propane, toluene, propylene, n-butane, etc. In the gas phase, providing superior advantages for complete oxidation. Large surface area $AMnO_3$ (A = La, Nd, Sm, Sr) perovskites were found to convert methane to CO_2 with 100% selectivity below 1023 K [15]. $LaMnO_3$, $La_{0.9}MnO_3$ and $LaMn_{0.9}O_3$ were tested in methane combustion in the temperature range of 475–600 °C and it was found that $LaMn_{0.9}O_3$ exhibited the highest performance in the complete oxidation of methane due to its large surface area as well as its defective structure being favorable for the development of active sites [16]. When the catalytic activity of $LaMnO_3$ produced by sol-gel, co-prepitation and glycine combustion techniques on toluene oxidation was evaluated, it was observed that $LaMnO_3$ produced by sol-gel exhibited better catalytic activity with specific surface area, reducibility at low temperature and concentration of oxygen species adsorbed on the surface [17]. The effect of AMnO3 (A = La, Sm) NPs prepared by combustion and hydrothermal synthesis on the selectivity of propane in the oxidative dehydrogenation of propane was investigated and it was observed that the increase in selectivity was related to the presence of Mn in the low oxidation state (2+/3+), the increasing concentration of hydroxyl groups on the particle surface and more active oxygen species adsorbed on the catalyst surface [18]. Among the 15 nm diameter $La_{0.9}K_{0.1}Co_{0.9}Ni_{0.1}O_3$ NPs synthesized by three different methods, namely sol-gel, self-combustion and microwave-assisted, the particles produced by sol-gel technique exhibited the best catalytic activity with 79% CO_2 selectivity due to having more oxygen activating species and being able to contact more incomplete combustion species due to their very small particle size [19]. Evaluation of the catalytic activity of $AFeO_3$-based A = (La, Nd) perovskite series on CO showed that relatively simple changes in the composition of the catalyst, such as changing the A-site cation (La^{3+} vs. Nd^{3+}) and/or increasing the content of the A-site dopant (10% or 40% Ca), greatly changed the activity and ignition temperature of the catalyst [20].

By changing the location and proportion of the components in the structure of perovskites, both their surface area and oxygen adsorption capability can be improved. They thus provide enhanced catalytic activity for the oxidation of hydrocarbons. These properties have recently made their direct use in conventional liquid hydrocarbon fuels attractive. The droplet-scale combustion behavior of gasoline-based nanofuels prepared by doping Fe_2O_3 and Fe_3O_4 NPs with 90–100 nm particle size distribution and $LaFeO_3$, $La_{0.5}Fe_{1.5}O_3$ and $La_{0.75}Fe_{1.25}O_3$ NPs with 25–40 nm size distribution were characterized [21]. The results showed that perovskites increase the flame temperature by allowing oxidation of incompletely burning radicals and the catalytic activity of the particles is improved by decreasing the La content in the A site and increasing the Fe content in the B site ($La_{0.5}Fe_{1.5}O_3$>$La_{0.75}Fe_{1.25}O_3$>$LaFeO_3$). Albeit, it has been shown that not only the large surface area and high oxygen content of perovskites in liquid fuels, but also the aggregation during combustion, transport to the flame zone and secondary atomization phenomena they cause have an impact on their performance.

Traditional hydrocarbon fuels such as gasoline continue to be used in many areas, such as gas turbine power plants, as well as in the public area. Its mixtures with kerosene are often used in gas turbine power plants. On the other hand, given the global climate crisis, their imperfect combustion characteristics, which lead to heavy soot formation and emissions, require their use in combination with additives with high oxygen content or energy value. There is no doubt that the use of low-cost and easy-to-produce perovskites to improve the combustion behavior of gasoline would be an important alternative. A review of the literature shows that perovskites based on $La_{1-X}A_XBMnO_3$ or $A_{1-X}B_XMnO_3$ partially or fully substituted with foreign cations, especially with high surface oxygen and Mn^{4+}/Mn^{3+} mobility, designed in different sequences, are the most suitable configurations for this purpose among NPs. In this study, $LaMnO_3$, $La_{0.7}Nd_{0.3}MnO_3$, $Nd_{0.7}Ba_{0.3}MnO_3$, $La_{0.7}Ba_{0.3}MnO_3$ and $La_{0.5}Nd_{0.3}Ba_{0.2}MnO_3$ perovskite type NPs were produced and their effect on the combustion behavior of gasoline at the droplet scale was evaluated. The microstructure and phase analysis of the produced NPs were performed by SEM and XRD techniques, respectively. The chemistry, surface area and spectral properties of the particles were determined by XPS, BET and UV–Vis analyses. Rietveld refinement and 3D visualization processes were applied to learn more about crystal parameters and morphology, respectively. Ignition and combustion processes of gasoline-based nanofuels were investigated. Ignition delay times, extinction times, and maximum flame temperatures were investigated during combustion processes. The effect of surface area and oxygen adsorption ability on catalytic activity is discussed.

2. Experimental methodology

2.1. Chemicals

Lanthanum nitrate hexahydrate ($La(NO_3)_3{\cdot}6H_2O$), Manganese(II) nitrate hydrate ($Mn(NO_3)_2{\cdot}4H_2O$) and Barium nitrate ($Ba(NO_3)_2$) have purchased from Chempur. Citric acid monohydrate ($C_6H_8O_7.H_2O$), ethylene glycol ($HOCH_2CH_2OH$), Lanthanum(III) oxide (La_2O_3) and Manganese(IV) oxide (MnO_2) have purchased from Merck. Neodymium Nitrate Hexahydrate ($N_3NdO_3{\cdot}6H_2O$), oleic acid ($C_{18}H_{34}O_2$) have purchased from Aldrich Chemistry. Barium oxide (BaO) has purchased from Alfa Aesar.

2.2. Perovskite type NPs synthesis and characterization

All Perovskite-type NPs were produced using the sol-gel technique. The main steps of the production process are summarized in Fig. 1 and the chemicals used for the production of each NP and their ratios are presented in Table 1. The same synthesis procedure was followed for all NPs. First, metal salts were dissolved in distilled water in a controlled manner in the ratios presented in Table 1. Then citric acid ($C_6H_8O_7.H_2O$) and ethylene glycol ($C_2H_6O_2$) were added to the mixtures in certain ratios as chelating agents. The resulting mixtures were boiled at 200 °C in a controlled manner until a viscous residue was formed. The residues were then dried at 250 °C until a dry gel was formed and finally burned in air at 600 °C for 12 h to remove organic matter formed during the chemical reaction process. The procedure we used for the production of perovskite-type NPs was described in more detail in our previous study [21].

Microstructures and surface morphologies of perovskite type NPs were determined by FEI-Quanta 650 field emission scanning electron microscope (SEM). Phase structures were analyzed with a Cu-Kα sourced Panalytical Empyrean X-Ray diffractometer (XRD) at a wavelength of $\lambda = 1.54$ A°. Measurements were taken at $2\theta = 20°–80°$ (for LBM, LNBM1) and $2\theta = 10°–90°$ (for LM1, LNM1, NBM) 0.02000° and 0.01313° steps at 300 K room temperature. The Rietveld refinement method was used with the help of the FullProf software to determine the crystal properties of nano-compounds from the obtained XRD diffraction data. The powder diffraction pattern obtained statistically using the least squares method is fitted to a curve in this method, allowing the structure of the compounds to be analyzed. The crystal structure of the components was determined by first performing the crystallographic characterization processes in FullProf software and then processing the obtained data with VESTA 3D visualization software. Surface area and micropore size measurements were performed at 77 K in a liquid nitrogen environment based on the N_2 adsorption technique. Optical properties were recorded on the Thermofisher ultraviolet–visible (UV–Vis) spectrophotometer. The chemical element states of the samples were characterized by X-ray photoelectron spectroscopy (XPS) with a monochromatized Al-Kα X-ray source.

2.3. Fuel preparation, experimental setup and visual analysis

Gasoline-based nanofuels were produced by mixing 2.5 %wt. perovskite type NPs and 1 %wt. oleic acid surfactant in an ultrasonic bath for 1 h [22]. The codes determined for the prepared nanofuel samples are presented in Table 2.

Two important considerations in the preparation of nanofuels are the concentration and homogenization of the components. The combustion behavior of nanofuels prepared at dilute and high NP concentrations is significantly different. Studies have shown that the average concentration for NPs doped into nanofuels is 2.5 %wt. Above this ratio, the nanofuel mixture is called highly concentrated, while below this ratio, it is called dilute concentrated. In this study, since the effect of the change in the design and stoichiometric ratios of the components of the perovskite type NPs used on the combustion behavior was investigated, the particle concentration was set at 2.5 %wt. to minimize the effect of changes in combustion behavior due to dilute and high concentration. On the other hand, the oleic acid (OA) surfactant concentration was also set at 1 %wt. to minimize the effect of nanofuels on combustion behavior.

When long-chain surfactant molecules bind to NP surfaces, they form an absorption layer around the particles, as seen in Fig. 2. Colliding NPs generate impetus to triumph over the lure of van der Waals. The amount of surfactant in nanofuels must be in concentrations sufficient to form a layer around each particle. Thus, NPs can remain stable, albeit for a short time. But excess surfactant will form macromolecules (a long chain group of molecules) that are free in solution and are called depletion stabilization [23]. This is undesirable as the main components of nanofuel are liquid fuel and NP particles. The appropriate concentration of the components is extremely important as the properties of the base fuels such as boiling point, viscosity, and surface tension will change in the presence of NP and surfactant.

Combustion experiments of GA, GA + OA NP-free and GA + LM1, GA + LNM1, GA + NBM, GA + LBM and GA + LNBM1 nanofuel in droplet scale were carried out in a rectangular prism chamber measuring 550 mm × 250 × 400 mm under stable atmospheric conditions (25 ± 5 °C, 1 atm, and relative humidity 53%). There are three openings in the chamber for optical access, backlighting, and temperature measurement. Fig. 3 illustrates the experimental setup of the 50 μm diameter wire configuration, synchronous spark generator-high speed camera, and thermal camera system for studying droplet live flame images and atomization mechanism. A 2 mm gap is left between the fuel droplets and the electric arc igniter to prevent them from coming into contact. A volume-calibrated single-channel micropipette (Variable volume "Micropipette Transferpette® " 0.5–10 μl) was used to produce constant volume droplets of 4.15 ± 0.25 μl to be suspended on the wire. The equivalent diameter of the suspended fuel droplets was calculated to be 2 ± 0.1 mm. Short duration (1 ms) and high energy (6 kV) sparks provided by an ignition transformer at 20 ms intervals ignited the fuel droplets suspended on the wire at atmospheric pressure. 11.5–69 mm Focal Length 2/3″ Format F1.4 Aperture M46 x P0.75 Filter Size Manual Iris Settings lens and 14000 fps Ditect HAS-EFC High-Speed Camera with 2560 × 2048 pixels image resolution, live flame images of droplets, change in diameters and used to record the atomization behavior. The lens settings are 11.5–69 mm focal length, 2/3″ format, F1.4 aperture, M46 x P0.75 filter size and manual iris. Between 400 and 800 nm wavelength, the transmission of the lens changes from 60% to 90%. The

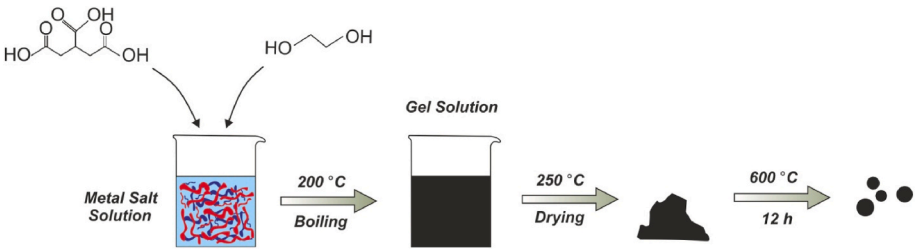


Fig. 1. The main production scheme of perovskite-type NPs.

Table 1
Quantities of chemicals used for NPs produced by sol-gel technique.

Chemicals	NPs				
	$LaMnO_3$	$La_{0.7}Nd_{0.3}MnO_3$	$Nd_{0.7}Ba_{0.3}MnO_3$	$La_{0.7}Ba_{0.3}MnO_3$	$La_{0.5}Nd_{0.3}Ba_{0.2}MnO_3$
$La(NO_3)_3{\cdot}6H_2O$ (g)	8.06	4.98	–	–	5.34
La_2O_3 (g)	–	–	–	4.72	–
$Mn(NO_3)_2{\cdot}4H_2O$ (g)	6.23	4.12	6.14	–	6.19
$N_3NdO_3{\cdot}6H_2O$ (g)	–	2.16	7.51	–	3.24
$Ba(NO_3)_2$ (g)	–	–	1.92	–	1.28
BaO (g)	–	–	–	1.91	–
MnO_2 (g)	–	–	–	10.3	–
$C_6H_8O_7{\cdot}H_2O$ (g)	104.2	69.01	102.81	174.01	94.77
$C_2H_6O_2$ (ml)	27.72	18.36	27.34	46.28	27.6

Table 2
Nanofuel mixtures.

GA	GA + OA	GA + LM1	GA + LNM1	GA + LBM	GA + NBM	GA + LNBM1
Gasoline	Gasoline +1% wt. oleic acid (OA)	Gasoline + 1% wt. OA + % 2.5 $LaMnO_3$ (LM1)	Gasoline + 1% wt. OA + % 2.5 $La_{0.7}Nd_{0.3}MnO_3$ (LNM1)	Gasoline + 1% wt. OA + % 2.5 $La_{0.7}Ba_{0.3}MnO_3$ (LBM)	Gasoline + 1% wt. OA + % 2.5 $Nd_{0.7}Ba_{0.3}MnO_3$ (NBM)	Gasoline + 1% wt. OA + % 2.5 $La_{0.5}Nd_{0.3}Ba_{0.2}MnO_3$ (LNBM1)

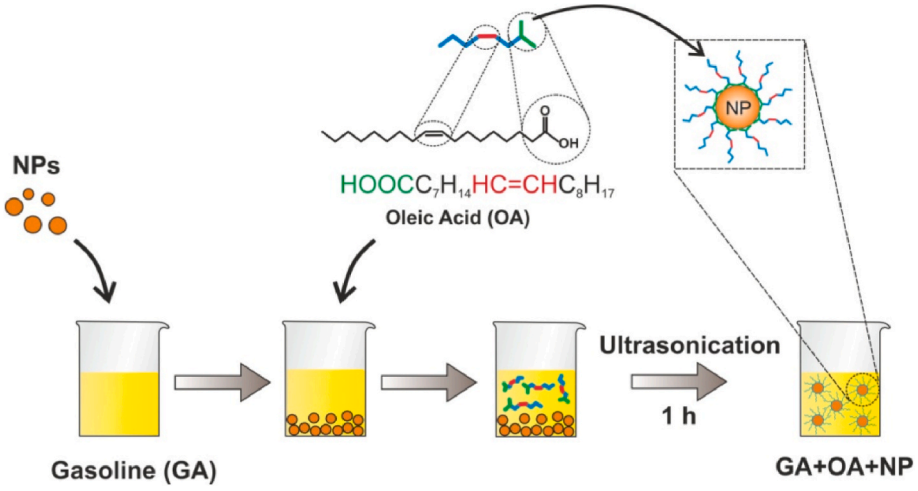


Fig. 2. Schematic representation of surfactant-coated perovskite-type nanoparticles.

live flame images of suspended droplets were recorded against a black background. The droplet was volumetrically illuminated during recording to fully capture the temporal development of important events such as bubble ejection, daughter droplet formation, and surface fluctuations. A FLIR E96 23° thermal camera at 640 × 480 thermal resolution and 7.5–14 μm spectral range with thermal sensitivity <40 mK at 30 °C (86 °F), error rate ±2 °C (±3.6 °F) or ±2% was used to detect changes in flame temperature and maximum flame temperatures. The lens contributes to the 23° × 18° field of view, and the thermal camera lens enables users to keep a safe distance from an energized point (approximately 3 m) while obtaining a crisp focus on smaller targets.

Finally, using Otsu's thresholding technique, the contrast of the recorded grayscale images of droplet diameters and droplet atomization was improved and converted to binary images [24]. To determine the cross-sectional area, the droplet shape was reconstructed using an edge detection routine built into the image analysis toolbox of MATLAB 9.4. Fig. 4 presents a schematic visual that summarizes the image analysis process. During the combustion process, these dynamic time series data were used to obtain the corresponding data for the instantaneous droplet diameter D (defined as the predicted area-equivalent sphere diameter). The droplet volume at the start was 4.15 ± 0.25 μl. The 0.1 mm change in droplet diameter was caused by the error margin of the micropipette used on the prepared volume. This difference was discovered by processing the images captured during the diameter optimization processes of the fuel droplet through Matlab's edge detection routine. The error rate of 1% on the droplet regression dimensionless ratio $(D/D_0)^2$ is the error rate that occurs as a result of including only 3 significant digits of the 7-digit decimal part of the D diameter value obtained from the edge detection routine. The deviation in the results obtained in the operations performed by taking into account 7 significant digits was used to calculate this ratio. The reported data are the result of experimental studies that were repeated three times for the live flame images of each droplet and three times for the determination of the droplet diameter change and atomization behavior, a total of six times (droplet diameter change and atomization phenomena were determined by analyzing the same images). The image processing process is described in detail in our previous work [25].

After image processing, the live flame images were used to determine the combustion behavior, ignition delay, and exhaustion times of the fuel droplets. The time elapsed between the image of the droplet recorded at the first shot of the igniter and the image in which the first ignition moment was recorded in the video recordings taken during the experiment for each droplet was used to calculate the ignition delay time. The time from the end of the video recording, which ends with the

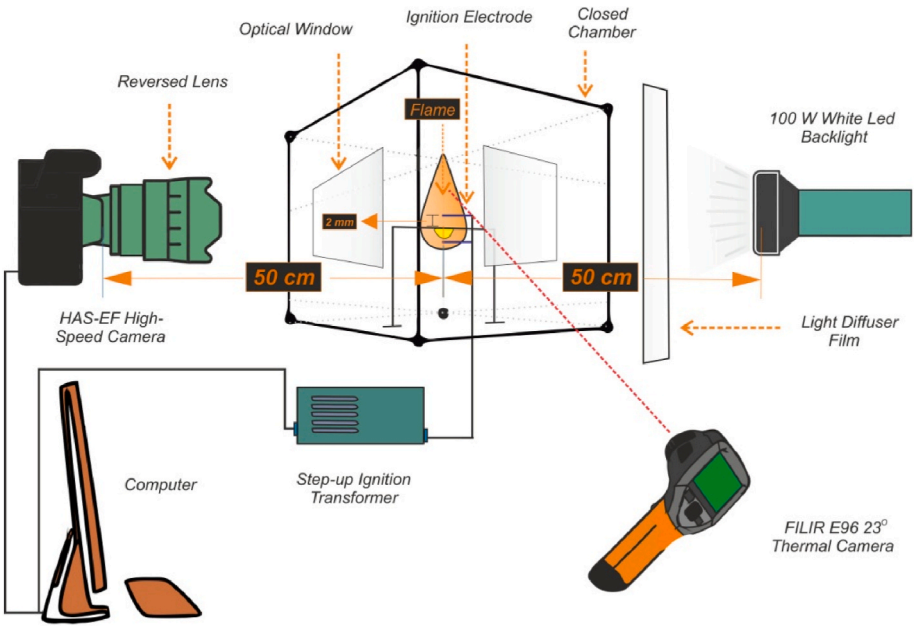


Fig. 3. Schematic representation of the experimental setup.

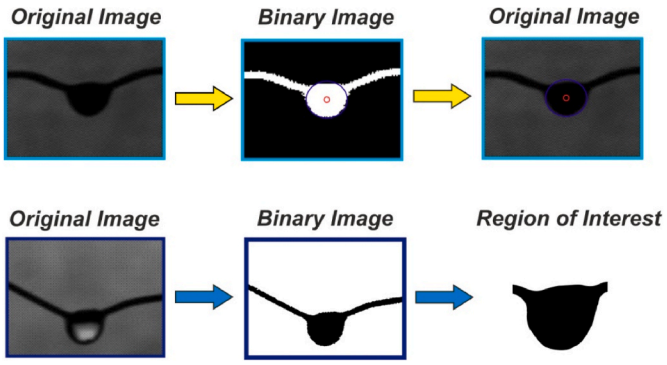


Fig. 4. Droplet image processing schematic for normal combustion (top) and droplet distortion (bottom).

capture of the last flame image of the fuel droplet, to the first ignition was used to calculate the extinction time. The localize maximum temperatures of the flame envelope were attempted to be determined in thermal camera images, and it was attempted to determine whether the increase in flame temperature was due to the formation of soot or the quality of the air-fuel mixture. Over a thousand droplet images were taken and analyzed for each droplet; sudden changes in the diameter of the fuel droplet during combustion were attempted to be observed, and the effects of atomization phenomena on the change in droplet diameter. The calculation and error rates of ignition delay and combustion times and the standard error rate of maximum temperature measurements have been described in detail in our previous studies [26,27].

3. Results and discussions

3.1. Characterization of perovskite type nanoparticles

Fig. 5 shows SEM images of LM1, LNM1, NBM, LBM, and LNBM1

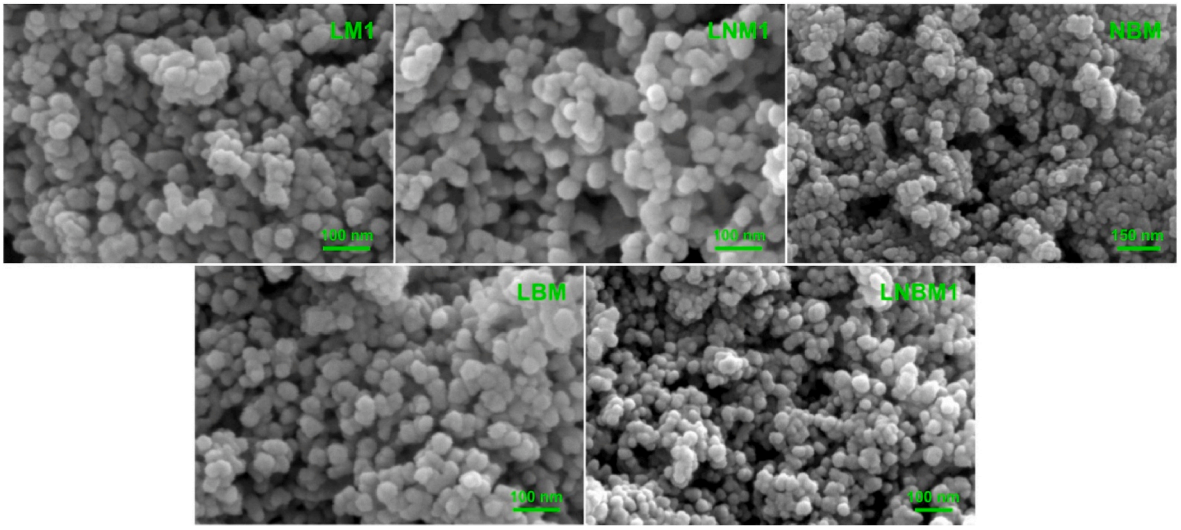


Fig. 5. SEM micrographs of LM1, LNM1, NBM, LBM, LNBM1 perovskite-type NPs.

perovskite-type NPs. Components substituted in varying proportions to $LaMnO_3$ perovskite-type NPs did not cause a significant increase in particle size, and the particle diameters of all samples were distributed in the range of 25–40 nm.

Experimentally measured XRD patterns and 3D lattice morphologies of LM1, LNM1, NBM, LBM, LNBM1 NPs are given in Figs. 6 and 7 as black dots. The XRD pattern calculated by Rietveld refinement according to the appropriate crystal symmetry is indicated by the red line. The obtained crystal structure parameters and the deviation amounts between the experimental result and the calculated value are given in Table 3. The crystal structure of LM1 NPs has lattice parameters a = 5.50179 Å, b = 5.50179 Å and c = 13.35940 Å in trigonal structure in R-3c crystal symmetry of the crystal structure. Less than 10% of the RF value of the LM1 (acceptance limit according to the literature) indicates that the obtained diffraction pattern is compatible with the calculated diffraction pattern. LNM1 NPs are in Pnma crystal symmetry and orthorhombic structure. The lattice parameters are a = 5.45610 Å, b = 7.73210 Å and c = 5.49930 Å. The RF value has increased above 10%. This is because the Nd substitution does not give a distinct peak in the diffraction pattern. The XRD model shows that the perovskite structure of the compound is preserved. Nd peaks were not included in the analysis because they remained in the noise. On the other hand, the volume of the unit cell was reduced compared to the LM1 sample. This is because, as expected, the atomic radius of the La atom is larger than the atomic diameter of the Nd atom (R_{La} = 250 p.m., R_{Nd} = 229 p.m.). Although LNM1 NPs have more components with Nd substitution compared to LM1 NPs, they contain 0.3 reduced La compared to LM1 and 0.3 Nd instead. Although Nd was added as much as the reduced La element, the difference between atomic radii caused the unit volume to decrease. 3D crystal structure images show that Nd substituent atoms with high oxygen vacancies induce changes in the morphology of LNM1 NPs.

LBM NPs have R-3c crystal symmetry, orthorhombic structure and lattice parameters a = 5.54330 Å, b = 5.54330 Å and c = 13.47100 Å. Ba substitution in the structure of LBM particles did not cause a significant change when compared to the XRD pattern of LM1. The crystal structure of NBM NPs with Nd on the A side and Ba on the B side of the perovskite structure have lattice parameters a = 5.47301 Å, b = 7.76418 Å and c = 5.52144 Å in orthorhombic structure in Imma crystal symmetry. The XRD pattern showed significant differences compared to LBM NPs. This is because the Nd element is located on the A side. However, the replacement of La atom by Nd atom also significantly changed the crystal structure of NBM compared to LBM NPs. These conditions have caused the RF value to exceed 10%. The crystal structure of LNBM1

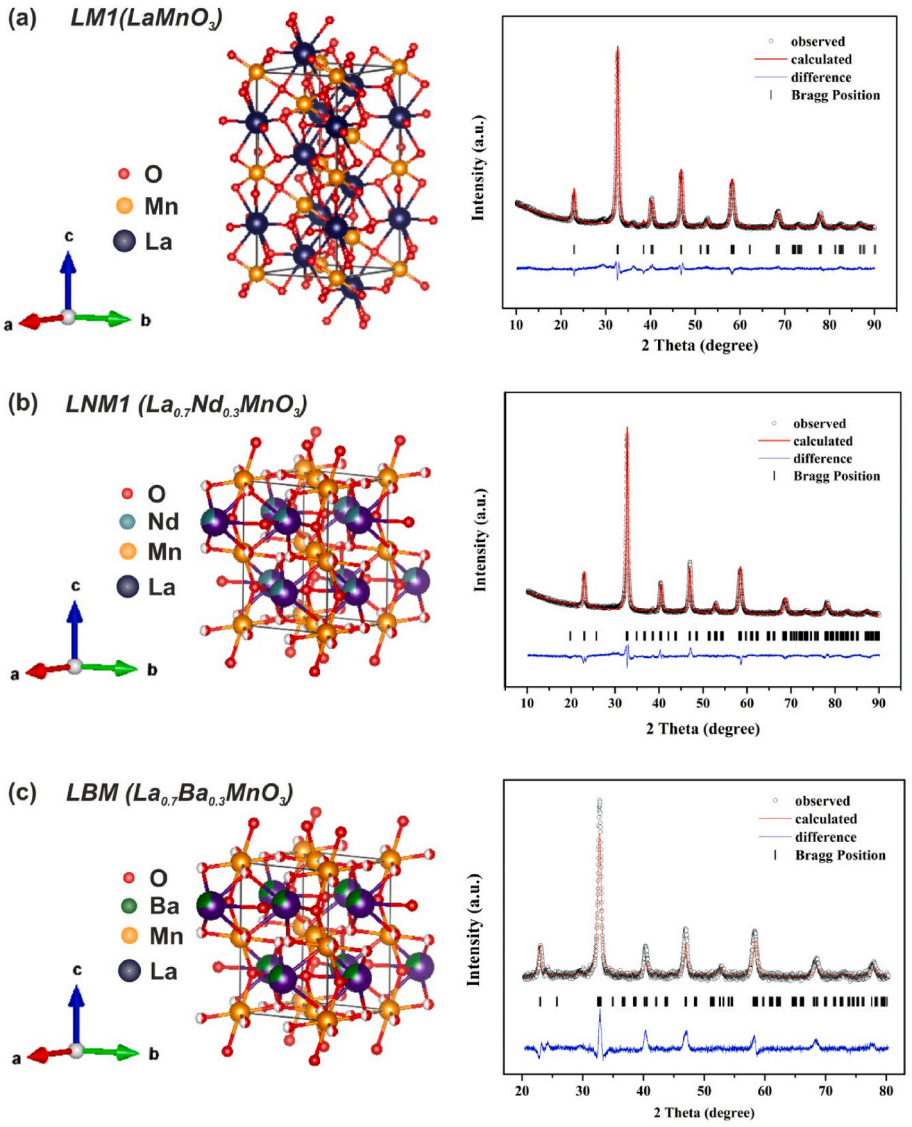


Fig. 6. Crystal structure and XRD diffraction patterns of LM1, LNM1 and LBM perovskite-type NPs.

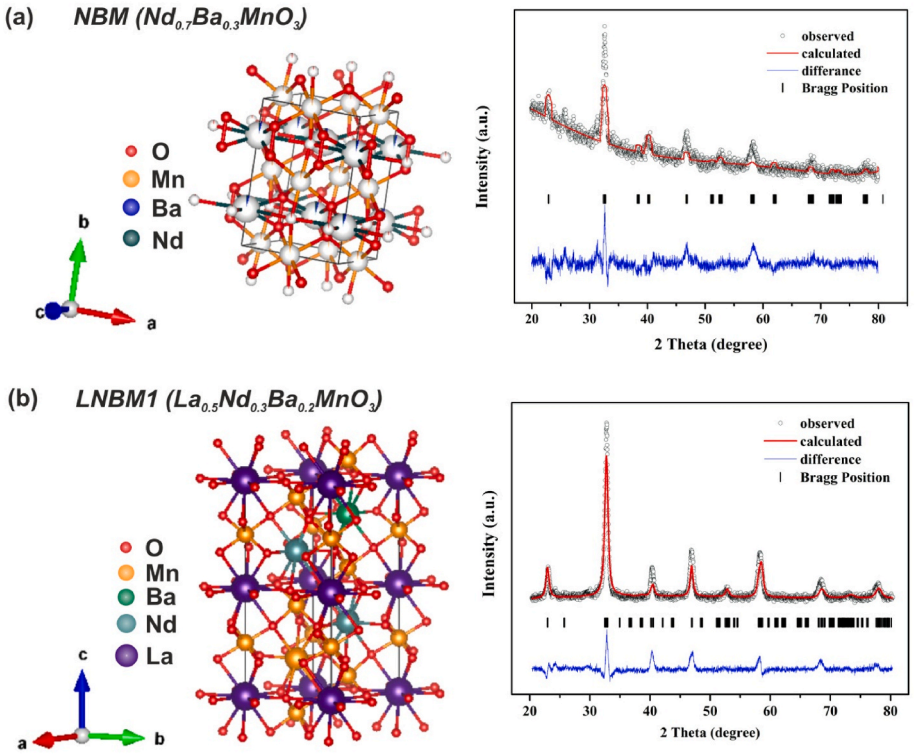


Fig. 7. Crystal structure and XRD diffraction patterns of NBM, LNBM1 perovskite-type NPs.

Table 3
Lattice parameters obtained by XRD Rietveld analysis and crystallographic characterization of perovskite type NPs.

	LM1	LNM1	NBM	LBM	LNBM1
Space Group	R-3c	Pnma	Imma	R-3c	Pnma
Crystal Structure	Trigonal	Orthorhombic	Orthorhombic	Orthorhombic	Orthorhombic
a (Å)	5.50179	5.45610	5.47301	5.54330	5.62322
b (Å)	5.50179	7.73210	7.76418	5.54330	5.62322
c (Å)	13.35940	5.49930	5.52144	13.47100	13.54033
V $(Å)^3$	350.2076	231.999578	234.624960	358.4819	370.791318
Chi	3.88	4.82	2.48	3.57	4.14
Rf Factor	5.670	24.6	61.75	12.53	51.1

nanoparticles has Pnma crystal symmetry similar to LNM1 NPs and is orthorhombic in structure. Nd and Ba substituents did not cause a change in the crystal symmetry and lattice structure of the perovskite structure. The crystal lattice parameters are a = 5.62322 Å, b = 5.62322 Å and c = 13.54033 Å. The volume of the unit cell increased due to the larger atomic diameter of the Ba atom (R_{Ba} = 268 p.m.) compared to the La and Nd atoms. Because the Nd and Ba elements did not exhibit a significant peak, the RF value increased.

Fig. 8 shows the overlaid diffraction patterns for comparison of NM1, LNM1, NBM, LBM and LNBM1 NPs. According to the standard XRD model of $LaMnO_3$ (JCPDS 01- 075–0440), the diffraction pattern in four different samples containing substitute elements appears to be similar to that of the unmodified sample [28]. Samples containing substituent atoms were successfully produced in orthorhombic structure without any impurities and/or secondary phases. As can be seen from Table 3, changes occurred in the crystal lattice parameters a, b, and c, and accordingly, the unit cell volumes in the crystal lattice, depending on the ratios of the substituting atoms and atomic radii.

Fig. 9 shows the UV–Vis absorption spectra, BET, and high resolution XPS spectrums results of the samples. The UV–Vis spectra in Fig. 9a show that UV light absorption in the 600–1100 nm range is significantly improved in the Nd-substituted LNM1 and NBM samples compared to the LM1 sample. Multiple oxygen vacancies can create imperfect energy

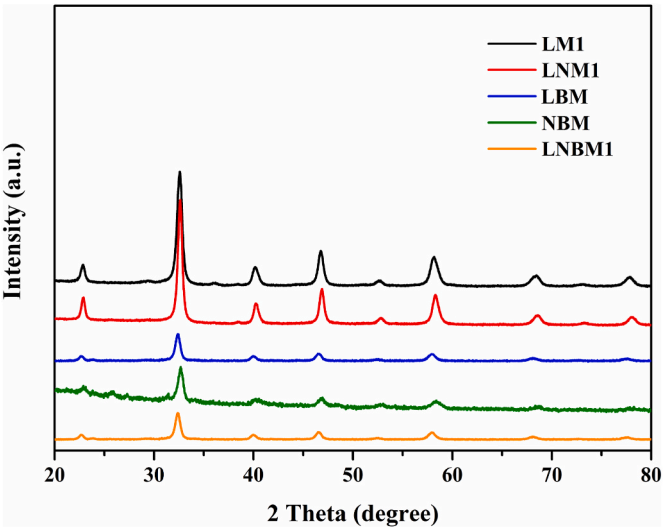


Fig. 8. XRD graphics of LM1, LNM1, NBM, LBM and LNBM1 perovskite-type NPs.

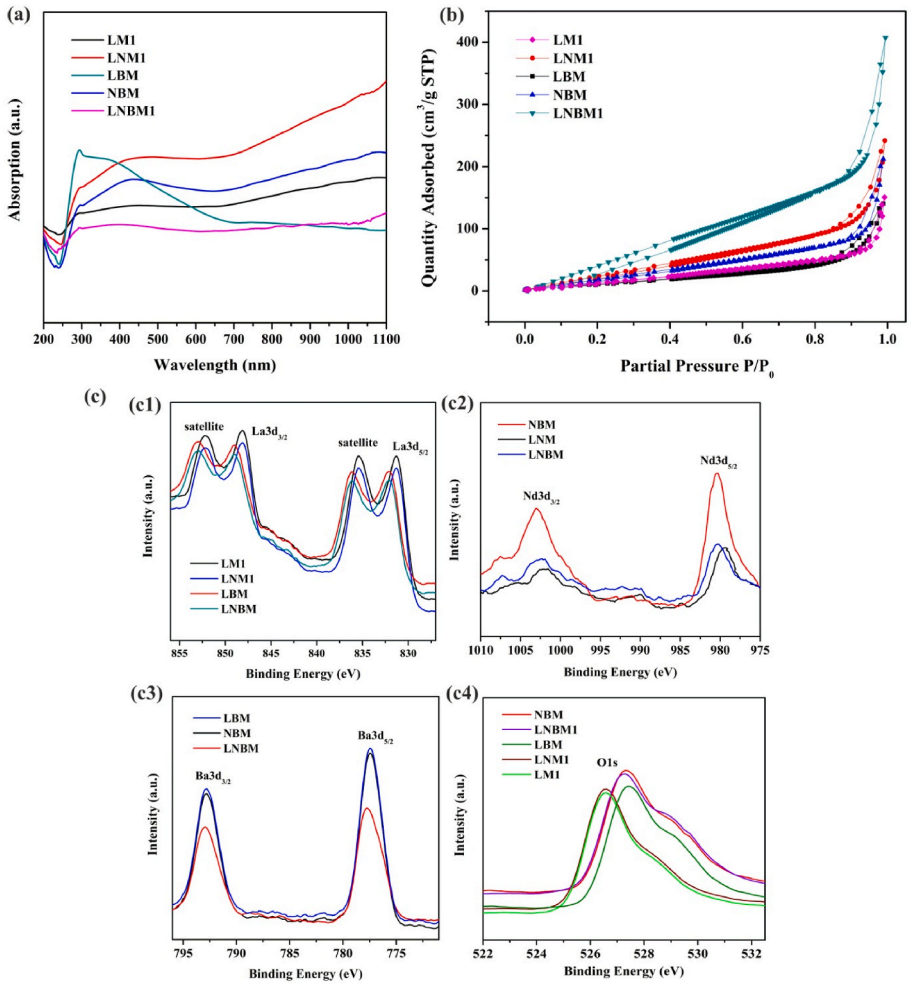


Fig. 9. a) UV–Vis spectra, b) BET and c) XPS analysis results of LM1, LNM1, NBM, LBM, LNBM1 perovskite-type NPs.

levels that narrow the band gap of the LNM1 sample and increase visible light absorption [29]. Nd substitution in the structure of the sample has the ability to form high oxygen vacancies. It is thought that the reason why the UV light absorption of NBM is lower compared to LNM1 is due to the low oxygen space creation energy of the substitute Ba in the sample. The gradual decrease in visible light absorption in other Ba substituted LBM and LNBM1 coded samples also supports this situation.

The adsorption-desorption curves and surface area and pore volume measurements of the samples are presented in Fig. 9b and Table 4, respectively. The highest surface area and pore volume for perovskite NPs were calculated for LNBM1 sample as 393.4898 m^2/g and 0.055287 cm^3/g, respectively. As expected, LM1 NPs were the particles with the lowest surface area. The increase in the surface area and pore volume values determined for the LNBM1 sample is an expected result due to the increase in the number of substituted elements in its structure. Because the substituted elements caused more defects to form in the structure of LNBM1, which resulted in a larger surface area [30].

High resolution XPS spectra of LM1, LNM1, LBM and LNBM1 perovskite type NPs containing La element are shown in Fig. 9c1. The binding energies of La $3d_{3/2}$ and La $3d_{5/2}$ orbitals in perovskites were estimated to be 848.2–849.1 eV and 831.3–832 eV, respectively (Fig. 9c1) [31]. This indicates that La ions essentially have a La3+ state. La 3d satellite peaks were observed at binding energies of 853.1–852.2 eV and 836.2–835.5 eV, respectively. This information about the core level of La indicates that La ions exhibit the +3 oxidation state. The decrease in La amount in the stoichiometric ratio showed itself with the decrease in the intensity of the peaks in the spectrum. LM1 NPs had the highest intensity peaks and LNBM1 particles containing the fewest La atoms in the stoichiometric ratio had the lowest density.

High resolution XPS spectra of LNM1, NBM and LNBM1 NPs containing Nd element are presented in Fig. 9c2. Nd The 3d spectrum shows bi-turn orbital properties at binding energies of 1003–1001.7 eV and 979.3–980.5 eV, respectively, attributable to the Nd $3d_{3/2}$ and Nd $3d_{5/2}$ components [32]. This finding is the Nd3+ oxidation state and indicates the presence of Nd. The energy differences between the peak rotation orbits are between 23 and 23.5 eV. This value is in good agreement with that reported in the literature (22.50 eV) [33]. The presence of 0.7 Nd in the structure of NBM NPs is manifested by a high-density peak. Ba $3d_{3/2}$ and Ba $3d_{5/2}$ can each be located with a peak at binding energies of 792.8 eV and 777.4 eV [34]. NBM and LBM NPs with the highest Ba content of 0.3 showed the highest peak intensity.

The O1s-binding energy region of LM1, LNM1, LBM, NBM, and LNBM1 perovskites reveals two distinct XPS peaks. Peaks at low binding energy are assigned to lattice oxygen (O^{2-}) at 526.6–527.3 eV, and peaks at high binding energy 528.2–528.8 eV are assigned to adsorbed

Table 4
The surface area and pore volume of LM1, LNM1, LBM, NBM and LNBM1.

Sample	Surface Area m^2/g	Pore volume cm^3/g
LM1	57.3531	0.015606
LNM1	156.2014	0.032368
LBM	65.825	0.010582
NBM	117.8164	0.025547
LNBM1	393.4898	0.055287

oxygen species [18]. The presence of Nd substitution elements NBM and LNBM1 increased the density of both the lattice oxygen and the adsorbed oxygen species. This evolution of the oxygen signal may represent different degrees of oxygen near the surface due to different surface areas.

3.2. Combustion of pure and surfactant-added fuel droplets

Figs. 10 and 11 show sequential flame images of pure gasoline (GA) and oleic acid doped (GA + OA) fuel droplets, respectively. Sequential flame images of OA-added gasoline droplets were recorded to evaluate the effect of the 1 % wt. OA additive on the combustion behavior of gasoline. The GA + OA droplet ignited $\tau = 0.001000$ s earlier than the GA droplet (Stage 1). This is because the ally group in the structure of monounsaturated oleic acid molecules slightly reduces the ignition delay [35]. As seen from the images in Stage 2, a flame envelope started to form around the droplet at similar times in both fuel droplets. After t = 300 ms of GA (Fig. 10 (vii-ix)) and t = 329 ms of GA + OA (Fig. 11 (vii-ix)), the flame envelope is fully developed. Both droplets exhibited a typical gasoline flame containing abundant incompletely burned hydrocarbons and soot. The increased flame brightness of GA + OA at t = 59 ms and t = 119 ms was due to the incomplete combustion of oleic acid, which has a higher ignition temperature than the base fuel, and after t = 239 ms, the flame brightness showed similarity with GA. However, the flame length of the GA + OA fuel droplet remained almost constant in the range of t = 428 ms and t = 1126 ms, which constitutes a large part of Stage 2 [36]. The reason for this may be related to the improvement in the air-fuel ratio due to the presence of OA and the need for less oxygen for the combustion of the GA + OA fuel droplet [37].

Stage 2 where stable flame envelope is seen for both fuel droplets is at similar time intervals (t = 501–851 ms for GA, t = 500–1126 ms for GA + OA). In the GA + OA droplet, low-intensity bubble ejections occurred at intervals of t = 741–750 ms (Fig. 11. (x-xii)). The reason for this is that the species with lower volatility are preferentially trapped in the center of the droplet in the GA + OA fuel droplet consisting of a binary liquid phase [38]. As the vapor pressure overcomes the droplet surface tension, these species were expelled from the droplet surface and moved to the flame zone by natural convection (Fig. 11. (xii)) [39].

Stage 3 is the part where the diameter reduction of the fuel droplets begins and is exhausted. The flame length of GA fuel droplets started to decrease at t = 962 ms, and the flame length of GA + OA fuel droplets at t = 750 ms. For the GA + OA droplet, the flame length did not change significantly in the range of t = 1166–1271 ms (xvi-xxi) and the combustion was accompanied by intense bubbe ejection events. This part represents the combustion of OA, which has a low ignition temperature compared to gasoline. The gasoline concentration in the droplet

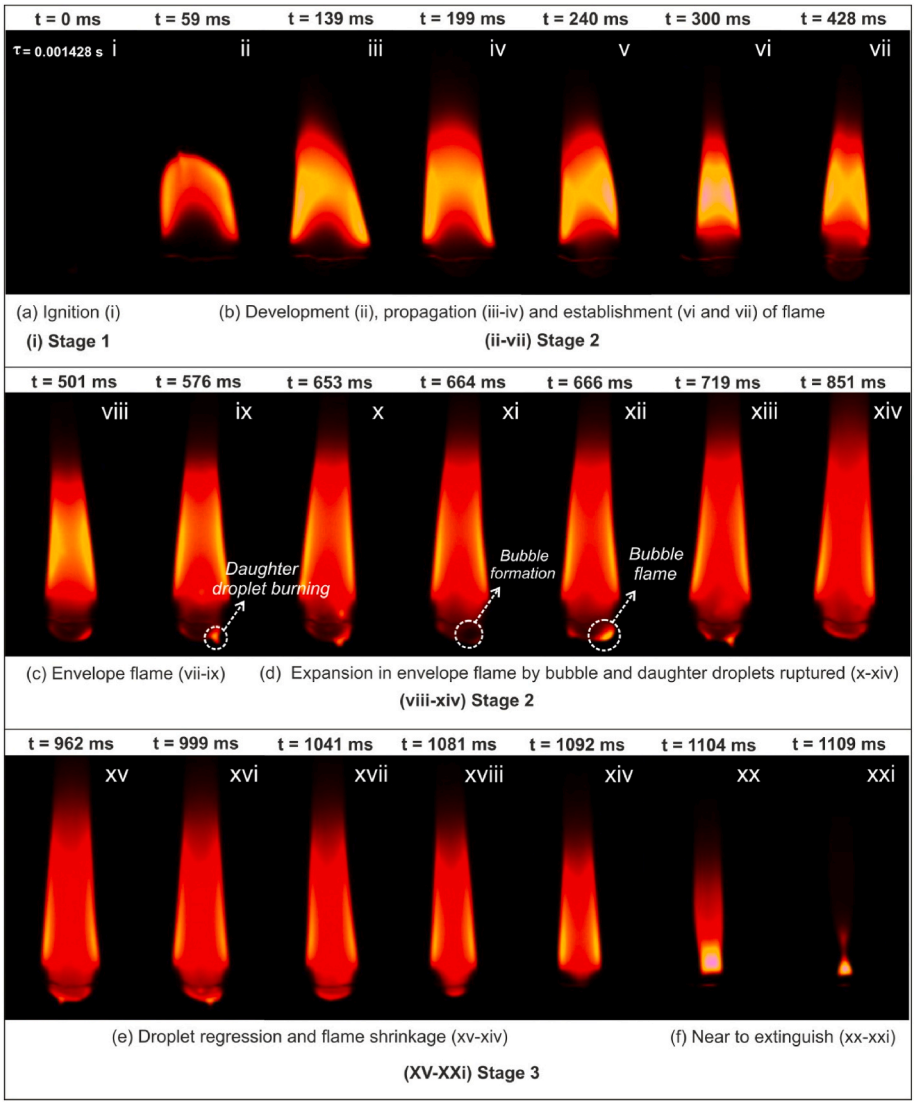


Fig. 10. Sequential flame images of GA fuel droplet.

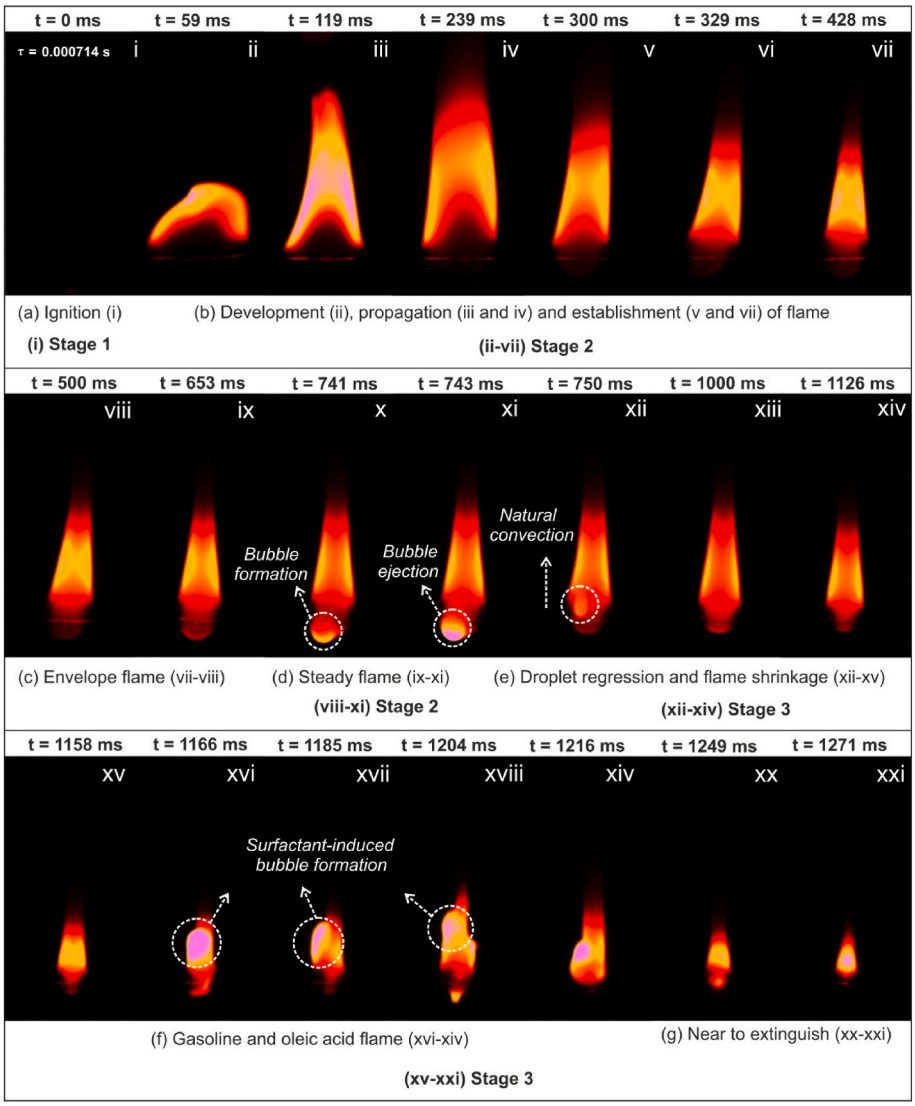


Fig. 11. Sequential flame images of GA + OA fuel droplet.

decreased towards the end of combustion. Bubbles were formed by the removal of the species trapped in the oleic acid agglomorate, which remained as a slurry due to this reduction. The removal of evaporating species from this structure with high surface tension requires higher vapor pressure. For this reason, the diameters of the bubbles thrown can be large and severe.

Fig. 12 shows the square of the normalized diameter of the GA and GA + OA fuel droplets as a function of time. Both fuel droplets exhibited severe volumetric shape oscillations due to internal boiling [24]. These oscillations put the parent droplet into a non-periodic cycle of swelling-contraction. This corresponds to fluctuations in the dimensionless droplet $(D/D_0)^2$ ratio in the normalized droplet regression curves. The entire lifecycle curve of a droplet consists of two phases, taking as the splitting point the moment when the droplet's reduction in diameter clearly begins. Stage 1 consists of the preheating process in which swelling-contraction and evaporation mechanisms compete with each other. When evaporation overcomes the swelling-shrinkage cycle, the droplet enters Stage 2 [40]. Due to the presence of OA, the GA + OA fuel droplet enters a large amplitude swelling-contraction cycle in Stage 1 compared to GA and the droplet diameter abruptly decreases. This is because the low volatility oleic acid migrates to the droplet surface due to the internal phase circulation and decreasing gasoline concentration within the droplet and does not allow the gasoline droplet to evaporate

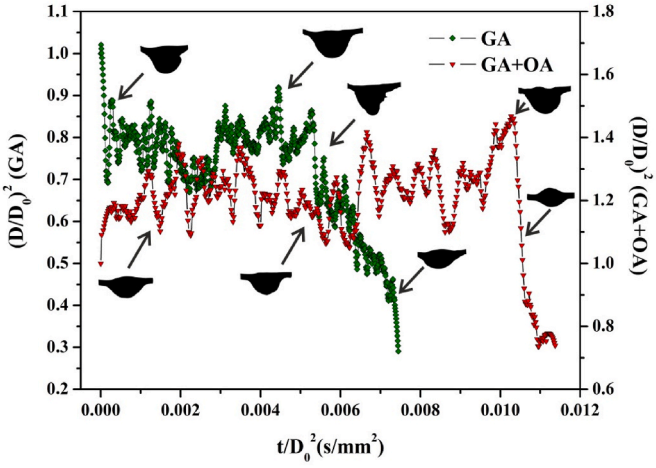


Fig. 12. The square of the normalized droplet diameter vs. normalized time for GA ve GA + OA nanofuels droplets.

[41,42]. As seen in Fig. 12, the initiation of diameter reduction after bubble ejection events, which occurs as a result of the internal vapor pressure overcoming the surface tension of the droplet, is proof of this. It is seen that there is no significant change in droplet diameter in the range of t/D_0^2 = 0.011–0.012 s/mm^2 of the GA + OA curve. This part represents surfactant combustion seen in Fig. 12 at the range t = 1166–1216 ms. In Fig. 13, the maximum flame temperatures of GA and GA + OA fuel droplets are presented. The addition of OA increased the maximum flame temperature of gasoline by only 1 °C. When the sequential flame images of GA and GA + OA fuel droplets and normalized droplet regression curves are compared, it is seen that the combustion behavior changes. In the tests carried out with NP additives, it was observed that as a result of the coating of OA on the surface of the NPs, an additional combustion process due to the presence of surfactant did not occur and the changes caused by OA on the gasoline droplet could be neglected.

3.3. Combustion of nanofuel droplets with addition of LM1 and LNM1 nanoparticles

The combustion behavior of nanofuels composed of dual-phase mixtures is characterized by the concentration and homogenization of add-on NPs, and the complex relationship of their physical and chemical properties with the atomization of the liquid phase and the combustion-evaporation mechanism. Gan and Qiao [41], defined five different stages in the combustion of n-decane and ethanol fuel droplets loaded with Al NPs: preheating and ignition, classical combustion, micro-explosion, surfactant flame, and Al droplet flame. Javed et al. observed four different regimes during the combustion of Al NP/heptane droplets and Al NP/kerosene droplets, namely ignition, vapor deposition, microexplosion, and surfactant flame [43,44]. They did not detect Al NP/n-decane classical combustion, Al drop flame or Al agglomerate combustion stages during the combustion of heptane and kerosene-based nanofuel droplets. They revealed that even before ignition, fuel droplets exhibit swelling-shrinkage behavior. In this study, the combustion process of gasoline-based nanofuels, whose sequential flame images are presented, consists of three stages: ignition (Stage 1), combustion with high kinetic energy droplet disruption phenomena (Stage 2), and combustion with low kinetic energy droplet disruption phenomena and diameter reduction (Stage 3).

In addition, Javed et al. reported that bubble and daughter droplet ejections characterize the droplet disruption mechanism during the development, propagation, and establishment of Al-NP/kerosene fuel droplet flames [43]. In gasoline-based fuel droplets containing perovskite type NPs, the disruption mechanism at this stage is evaporation occurring only on the droplet surface. Albeit, the formation of the luminous spherical flame region around GA and GA + OA fuel droplets started at about t = 300 ms after ignition, but occurred much later in fuels containing perovskite type NPs. All nanofuel droplets have the characteristic yellow-orange flame envelope color.

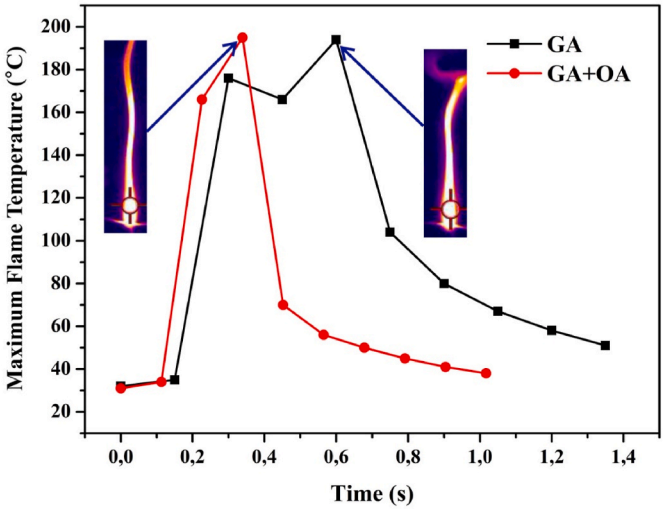


Fig. 13. Maximum flame temperatures of GA and GA + OA fuel droplets.

Another important difference is the presence of high kinetic energy droplet disruption phenomena and low kinetic energy droplet disruption phenomena in the combustion processes labeled as Stage 2 and Stage 3, respectively, in nanofuels containing NPs. In Stage 2, volumetric oscillations, surface fluctuations, bubble ejections, and particle transport are dominant, while in Stage 3 these formations are less numerous and more destructive. The microexplosion phenomenon, on the other hand, manifests itself as weak explosions at the beginning of Stage 3 and as powerful explosions at the end. This disruption mechanism in gasoline-based nanofuel droplets is compatible with the secondary atomization mechanism presented by Miglani et al. in their study in which they investigated the deformation mechanism of ethanol fuel droplets loaded with TiO_2 NPs [39].

Fig. 14 shows sequential combustion images of a GA + LM1 fuel droplet containing $LaMnO_3$ NPs. As of t = 470 ms (vii), daughter droplet ejections with high kinetic energy, free from particles, and much smaller in diameter than the base fuel droplet have started. These droplets, which are very slightly loaded with particles, do not have a disruptive effect in the flame envelope and are transported quite rapidly through the natural convective area. Daughter droplet ejections starting at t = 530 ms (viii) have low kinetic energy, particle load, and relatively larger diameters. As of t = 595 ms (x), large bubble ejections have started. The heterogeneous layer that nanoparticles started to form on the surface due to the internal phase circulation significantly changed the atomization mechanism [24,41]. This increased the number of bubbles formed by volatile species in the vapor phase trapped in the droplet, and their possibility of coalescence. The volumetric oscillation that started with the increasing internal pressure caused the ejection of NP-loaded daughter droplets and large bubbles from the droplet. These formations can have devastating effects, but their kinetic energy is low [45]. The fluctuations on the $(D/D_0)^2$ square curve of GA + LM1 in the range of $t/(D_0)^2$ = 0.000–0.003 (s/mm^2) in Fig. 16 show more clearly the swelling-shrinkage effect of bubble formations on the droplets. Gasoline is now transported to the flame zone by internal phase diffusion, as well as by bubble ejections and large daughter droplet ejections. As seen at t = 705 ms (xii), these formations, which have a disruptive effect on the flame region, on the other hand, cause the secondary atomization of the fuel droplet, causing the flame length to prolong in Stage 2 and the flame width to increase over time.

Due to the micro-explosion event that started at t = 810 ms (xiv), the droplet diameter has now entered the reduction phase and Stage 3 has begun. In Fig. 14, the sudden decrease in diameter at t/D_0^2 = 0.0025 (s/mm^2), and then the start of diameter regression confirms this situation. The first micro-explosion shows that the aggregated NPs on the fuel droplet surface now form a semi-solid shell. The bubbles formed by the fuel vapor, which can no longer diffuse from the droplet surface in the fuel droplet, will have to be expelled from the droplet surface with higher pressure in order to overcome the surface tension. This event caused intense gas release and combustion as seen in the instantaneous flame image at t = 818 ms (xv). The developing fuel-air mixture momentarily enlarged the flame envelope and better combustion of the species was achieved. While the droplet diameter continued to shrink, severe micro-explosions at t = 955 ms (xvi), t = 1135 ms (xviii), and t = 1215 ms (xiv) caused agglutinate nanoparticles to be transported to the flame region with high momentum and burned. However, the oleic acid chains attached to the surface of the NPs were also transferred to the flame zone and no additional surfactant combustion stage was observed. The snapshot at t = 1300 ms is the flame of agglutinate NPs.

In Fig. 15, sequential flame images of GA + LNM1 nanofuel droplets containing $La_{0.7}Nd_{0.3}MnO_3$ NPs are presented. After ignition, the GA +

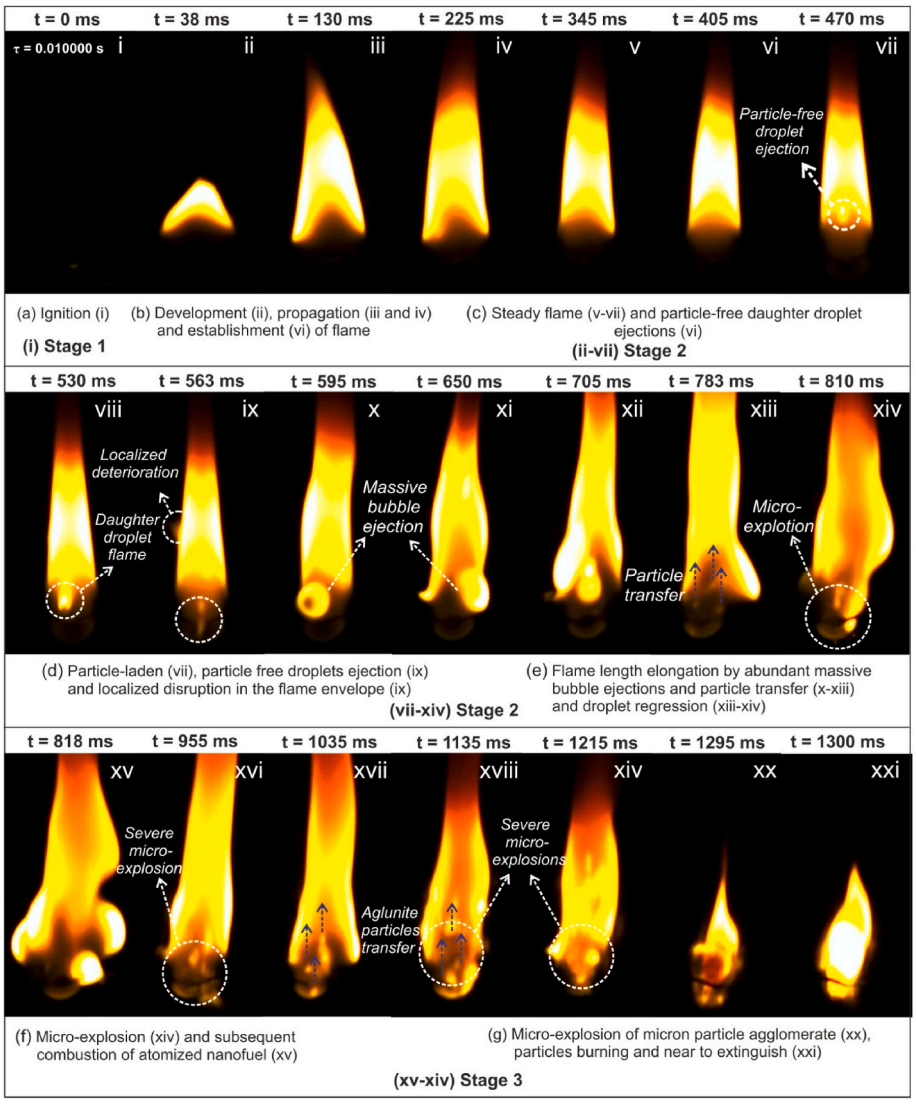


Fig. 14. Sequential flame images of GA + LM1 nanofuel droplets.

LNM1 flame has a shorter length and a narrower tail compared to the GA + LM1 flame envelope during the development, propagation, and establishment processes. The GA + LMN1 flame envelope is stable up to t = 531 ms (vii). Droplet disruption, which started with daughter droplet ejections at t = 698 ms (vii) and particle transports starting at t = 910 ms (x), left its place to more severe daughter droplet ejections as of t = 1051 ms (xii). Remarkably, bubble formations are rare in Stage 2, and ejections with high kinetic energy during this stage caused progressive enlargement and expansion of the flame envelope in GA + LMN1. Stage 3 is characterized by medium to high-density micro-explosions that begin with a violent micro-explosion at t = 1361 ms (xv), as can be seen from the flame images. The sudden diameter regression at $t/D_0^2 = 0.0049$ (s/mm^2) in the droplet regression curve of GA + LMN1 in Fig. 14 more clearly shows the strong microexplosion effect.

3.4. Combustion of nanofuel droplets with addition of LBM, NBM and LNBM1 perovskite type nanoparticles

Figs. 17 and 18 show sequential flame images of GA + LBM loaded with $La_{0.7}Ba_{0.3}MnO_3$ NPs, GA + NBM fuel droplets loaded with $Nd_{0.7}Ba_{0.3}MnO_3$ NPs, respectively. In Fig. 15, GA + LBM flame images are very similar in shape to GA, a pure gasoline droplet without NP. The change in flame color can be associated with the absence of Nd in the NP structure (The fact that Nd is used instead of La on the A side of the perovskite NP in Fig. 18 and that the flame color is quite similar to that in Fig. 15 confirms this situation). However, at t = 594.3 ms (vi), it exhibits a very similar burning behavior to the GA sample, except for the daughter droplet ejections and bubble ejections. The regression curve of the GA + LBM droplet in Fig. 19 is similar to the regression curve of the GA droplet in Fig. 12, which is also consistent with this situation. This is because these particles are not transported homogeneously to the flame zone and their aggregation propensity is very high.

When the live flame images of GA + NBM nanofuel droplets loaded with $Nd_{0.7}Ba_{0.3}MnO_3$ NPs in Fig. 18 are examined, it is seen that the GA + LNM1 fuel droplet in Fig. 15 is quite similar to the flame images. It is quite similar to the GA + LMN1 droplet in that the daughter droplet ejections start at t = 534 ms (vii) and the active droplet disruption mechanism during Stage 2 is the daughter droplet ejection. Albeit, towards the end of Stage 2, the maximum elongation and expansion in flame lengths between t = 843–938 ms are relatively larger than GA + LNM1. On the other hand, it is similar to the GA + LBM droplet in that high kinetic energy deformation events do not occur much. Bubble ejection events, which were active from the end of Stage 2, continued from t = 1124 ms (xv), and micro-explosions at t = 1409 ms (xvii) and t = 1497 ms (xviii) characterized Stage 3. The flame image at t = 1669 ms shows that agglomerated particles remain on the wire, which indicates

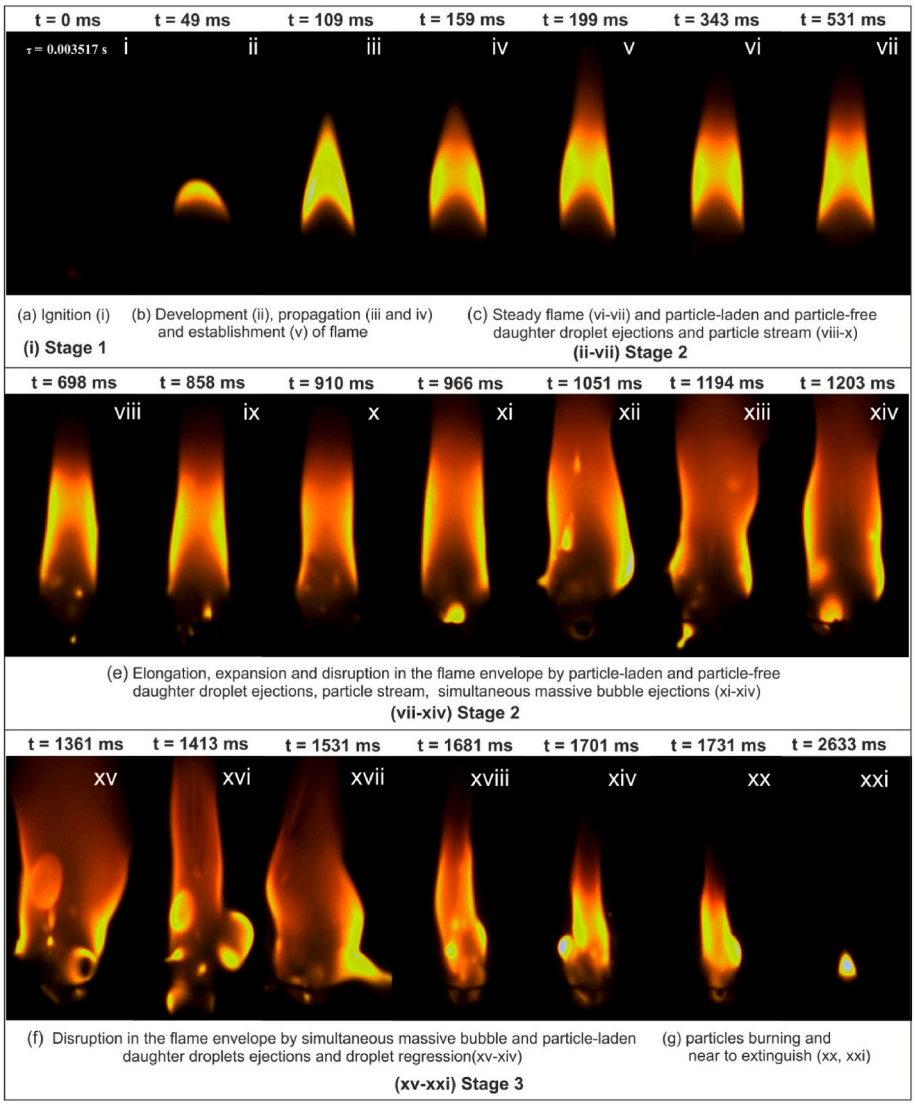


Fig. 15. Sequential flame images of GA + LNM1 nanofuel droplets.

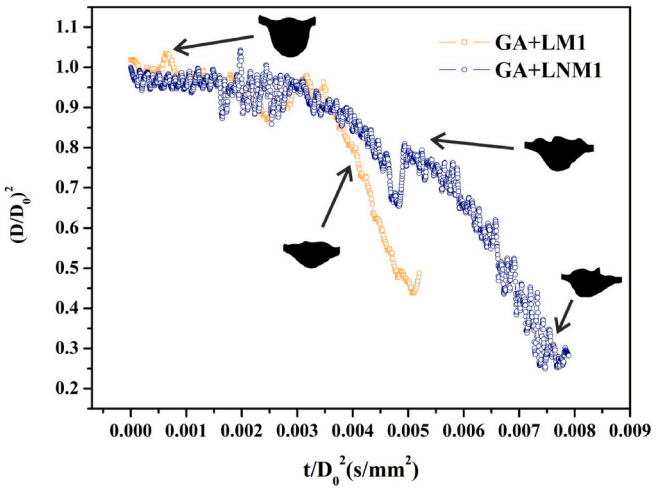


Fig. 16. Droplet regression plots of GA + LM1 and GA + LNM1 fuel droplets.

that the particles have a high tendency to agglomerate.

In Fig. 20, it was seen that it was ignited with a violent explosion event lasting up to t = 79 ms (ii) after ignition. This is thought to be due to the rather large surface area and imperfect surface properties of the LNBM1 particles (discussed in detail in section 3.5). The explosion caused the daughter droplet ejections and the particles to be transported to the flame region as of t = 587 ms (v) in Stage 2. The flame length, which started to increase after t = 637 ms (vi), continued until t = 1107 ms (xiii). The flame envelope formed is much longer and more stable than the flame of all other fuel droplets. It can be seen that the micro-explosion events are not very intense during the droplet lifetime, but as of t = 853 ms (ix), the relatively denser agglutinated particle is transported to the flame region. It is thought that the reason for this is the decrease in the concentration of the gasoline in the droplet, which is atomized and a large part of which is burned as a result of the explosion that occurs after the ignition. After this period, no destructive droplet disruption event was observed in the fuel droplet entering Stage 3 at t = 1107 ms (xiii). When the regression curve of GA + LNBM1 is examined in Fig. 19, the fact that only successive swelling-shrinkage events occur in the region where the diameter decrease starts confirms this situation. The reason for this is that a significant portion of the particles form agglutinates on the wire. The vigorous micro-explosion event at t = 1554 ms (xx) indicates that the semi-solid agglutinate was disintegrated.

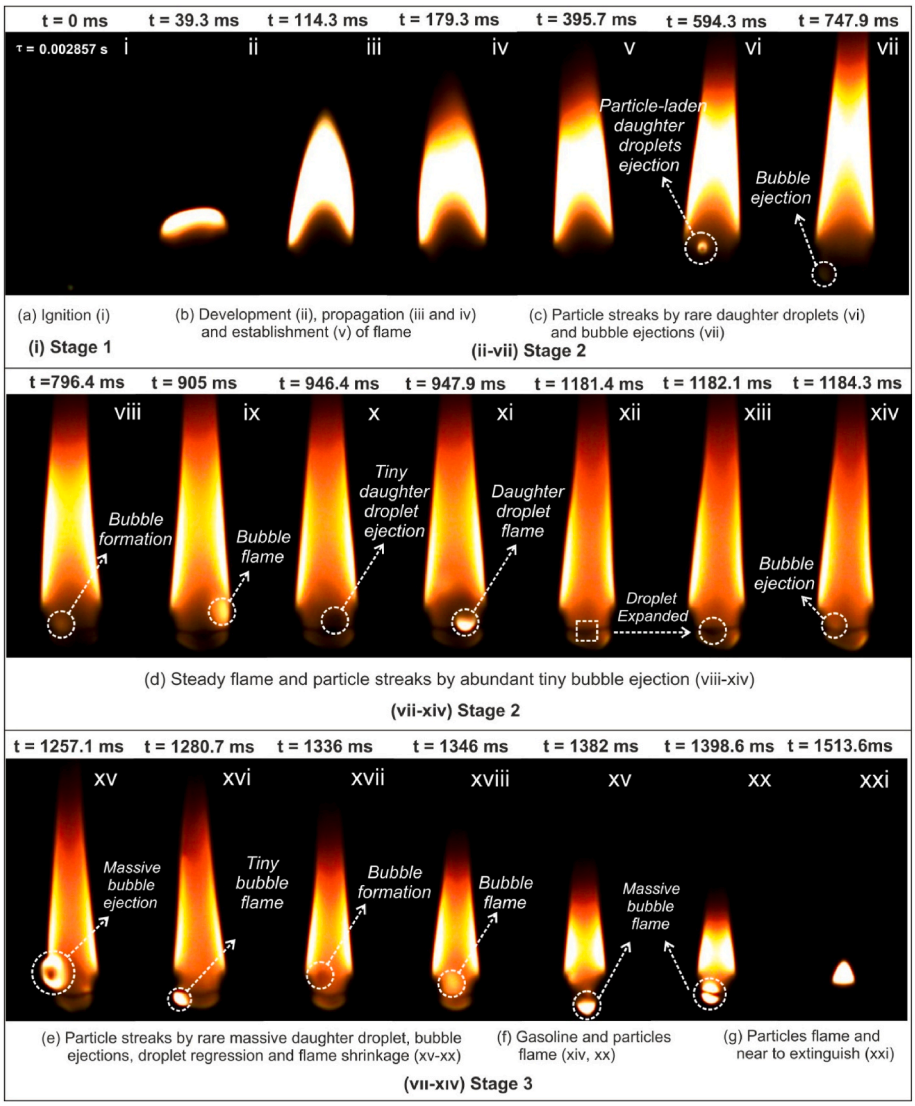


Fig. 17. Sequential flame images of GA + LBM fuel droplets.

As of t = 1554 ms (xx), only NPs burned and lasted for about 200 ms.

All perovskite type NPs increased the ignition delays compared to pure gasoline. The ignition delays of GA, GA + OA, GA + LM1, GA + LNM1, GA + LBM, GA + NBM and GA + LNBM1 droplets are 0.001428 s, 0.000714 s, 0.01000 s, 0.003517 s, 0.002857 s, 0.005000 s and 0.0011429 s, respectively. The reason for the low ignition delay of LBM particles is that, as already mentioned, they have no effect on the combustion of gasoline. However, GA + LNM1 and GA + NBM droplets containing LNM1 and NBM particles were the fuel droplets with the closest ignition delay to pure gasoline. As discussed in Section 3.1, these particles have both enhanced oxygen adsorption ability and large surface areas. Increased oxygen content increases the ignition delay, but the increased surface area of these particles compared to LM1 is thought to reduce the ignition delay. Because the large surface area provides an area for the continuity of combustion reactions. Although the LNMB1 fuel droplet had the largest surface area, the ignition delay of the GA + LNBM1 fuel droplet was slightly longer. The reason for this is thought to be the presence of functional groups containing a lot of oxygen on the surface.

3.5. Catalytic activity of perovskite-type NPs on droplet diffusion flame

The most important difference of gasoline-based nanofuels containing perovkit-type NPs from droplets GA and GA + OA NPs-free is the increase in the density of the non-luminous region after ignition. This is because perovskite-type oxides containing transition metals exhibit high catalytic activity for the oxidation of hydrocarbon fuels and volatile organic compounds [17,18]. In the perovskite-type oxide represented by ABO_3, the B-site cation is octahedrally surrounded by oxygen, and the A-site cation resides in the space formed by these octahedra. In this oxide system, the replacement of A and/or B site cations with other metal cations often leads to the formation of lattice defects [30]. Such defects are associated with high catalytic activity. Perovskite-type oxides partially substituted in the A and/or B sites desorb or adsorb large amounts of oxygen [46,47]. The nature and reactivity of adsorbed oxygen can differ greatly from other oxygen forming a solid crystal lattice because adsorbed oxygen binds to metal cations more weakly than normal lattice oxygen. Such weakly bound oxygen is considered effective in completing combustion [48].

On the surface of perovskite-type oxides, the two oxygen species α and β are combined with different bond strengths [30]. It is believed that α-oxygen, which is adsorbed and accommodated by dissociation in the oxygen vacancies with the formation of adjacent high-valent metal ions, is more active [16]. They also react with hydrocarbons at lower temperatures than the original lattice oxygen [15]. At low temperatures, when the activity of the lattice oxygen is negligible, the reaction is

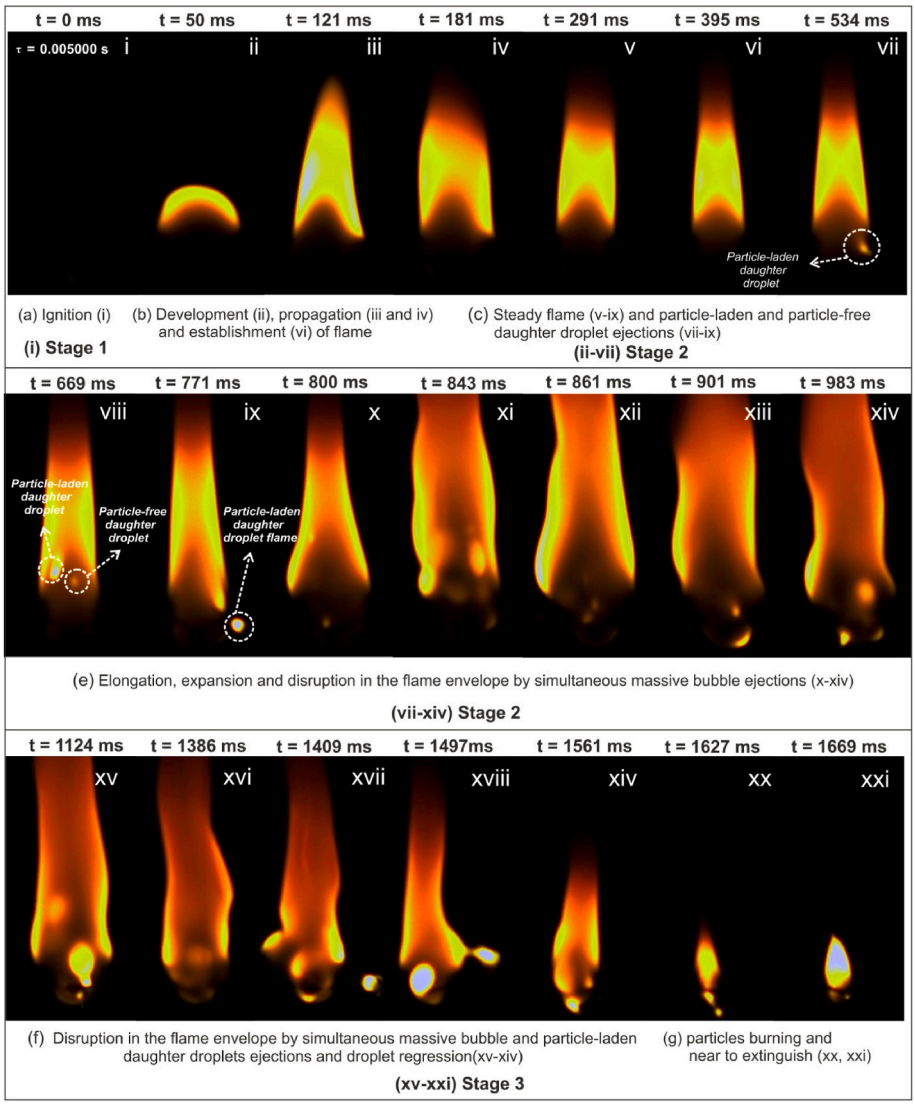


Fig. 18. Sequential flame images of GA + NBM fuel droplets.

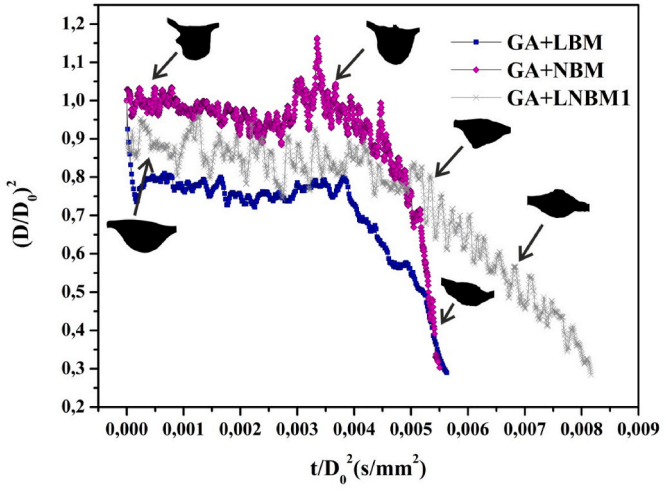


Fig. 19. Regression plots of GA + LBM, GA + NBM and GA + LNBM1 fuel droplets.

mainly driven by the adsorbed oxygen. The increase in the reaction temperature makes the β oxygen, that is, the normal lattice oxygen, reactive. Consequently, in this case the high temperature oxidation is predominantly driven by the lattice oxygen [30].

For catalysis applications in oxygen reduction reactions, only alkaline-earth and rare-earth metals are popular A-site cations [49]. The difference in the composition of the A-site cation will cause differences in the crystal structure and electronic structure of the perovskite, thereby affecting its activity in oxygen reduction reactions. Hyoda et al. showed that the activity of rare earth metals as A site elements in ABO_3 perovskite oxides follows La > Pr > Nd > Sm > Gd > Y > Dy > Yb [50]. La-containing perovskite oxide has the highest catalytic activity because La has the largest ion radius, resulting in the most suitable crystal and electronic material [48]. B-region cations are generally transition metals with incompletely filled d orbitals, especially incompletely filled 3d orbitals [51]. The B-site cation in a perovskite oxide plays a more important role than the A-site cation. This is because redox reactions usually occur in the B region.

$LaMnO_3$ is a typical perovskite with an excess of oxygen [52]. After ignition, the non-luminous region of the GA + LM1 flame containing $LaMnO_3$ NPs in Fig. 14 is more intense compared to the GA and GA + OA flames, and the luminous flame envelope around the droplet did not form until t = 478 ms. However, it can be said that the non-luminous

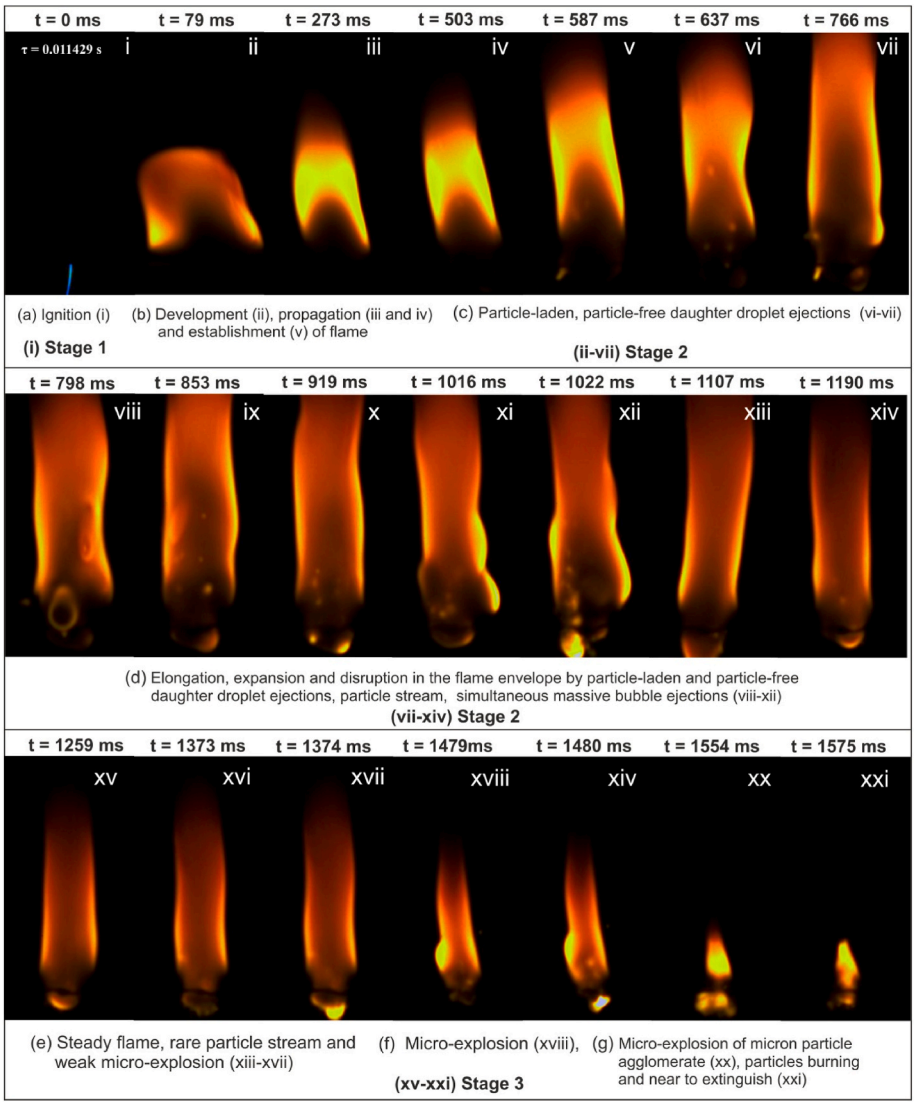


Fig. 20. Sequential flame images of GA + LNBM1 fuel droplets.

region, which is an indicator of high oxygen content, is relatively more developed. This is a sign of a relatively better fuel-air mixture. $LaMnO_3$ is known to show enhanced catalytic activity due to its enhanced surface area, porosity, surface Mn^{4+}/Mn^{3+} ratio (Mn^{4+}/Mn^{3+} and Mn^{3+}/Mn^{2+} redox pairs) and active oxygen species. It has been reported that it can exhibit good catalytic activity for the oxidation of toluene, methane and propane [15,17,30,53]. In Fig. 21, it is seen that the maximum flame temperature of the GA + LM1 fuel droplet increased by 35 °C compared to GA and GA + OA in Fig. 13. This can be attributed to the complete combustion of incompletely combusted hydrocarbons in the presence of oxygen during the pyrolysis of hydrocarbons. Complete combustion raises the flame temperature. In addition, during Stage 2 and Stage 3, LM1 NPs are continuously transported to the flame region by daughter droplets and bubble ejections and micro-explosions, indicating that it maintains its catalytic activity in this region as well.

Compared to $LaMnO_3$, $La_{0.7}Nd_{0.3}MnO_3$ NPs in GA + LNM1 droplets exhibited better catalytic activity due to the absence of luminous flame envelope around the droplet from t = 49 ms to t = 966 ms, and the formation of a higher non-luminous region. In addition, the shortening and tapering of the flame envelope between t = 49 ms and t = 139 ms is an indicator of increased oxygen content. The fact that the flame temperature rises by 50 °C compared to the additive-free fuel droplets and the flame temperature is 15 °C higher compared to GA + LM1 indicates that soot oxidation increases. The decrease in the brightness of the flame color supports this situation by indicating that the formation of soot decreases. This improvement is due to the substitution of the A region atoms of $La_{0.7}Nd_{0.3}MnO_3$ with Nd. Cation substitutions in perovskite oxides by substitution of A and/or B region atoms with a dopant element are an effective approach to creating oxygen vacancies. From the absorption curves presented in Fig. 9a, it can be seen that $La_{0.7}Nd_{0.3}Ba_{0.2}MnO_3$ NPs are the particles with the most advanced oxygen adsorption ability among all particles. However, the surface area of $LaMnO_3$ NPs (156.2014 m^2/g) is more than twice the surface area of $LaMnO_3$ NPs (57.3531 m^2/g) (see Table 4). The enhanced surface area provides a draft for combustion reactions to occur.

In general, A-site cation substitution tends to produce oxygen vacancies, while B-site cation substitution mainly causes electronic structure changes without generating oxygen vacancies [49]. Papa et al. [54], reported that neodymium-substituted zinc ferrites exhibit high catalytic activity for methane combustion. They noted that octahedrally coordinated Nd^{3+} ions have an important contribution to the formation of new types of defects useful for methane combustion. GA + LBM and GA + NBM fuel droplets containing Ba-substituted $La_{0.7}Ba_{0.3}MnO_3$ and $Nd_{0.7}Ba_{0.3}MnO_3$ perovskite oxides caused the flame temperatures to increase only by 12 °C and 15 °C, respectively, compared to pure fuels. They also have a less developed dark region compared to GA + LMN1.

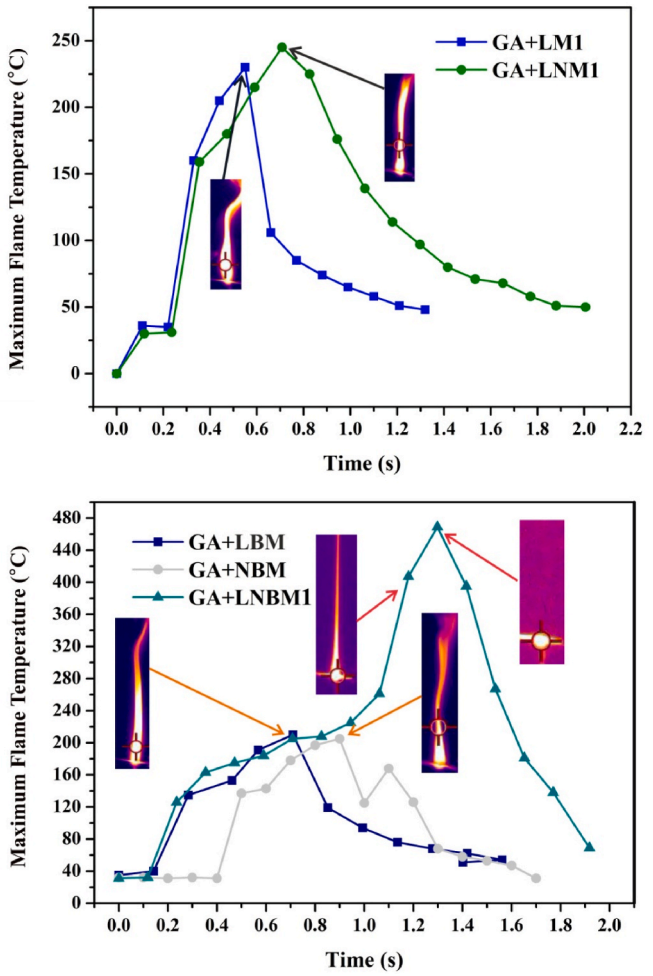


Fig. 21. Maximum flame temperatures of GA + LM1, GA + LNM1, GA + LBM, GA + NBM and GA + LNBM1 fuel droplets.

The absorption spectrum, adsorption-desorption curves and surface area measurement value (65.825 m^2/g) of $La_{0.7}Ba_{0.3}MnO_3$ presented in Fig. 9a and b and Table 4, respectively, show that its catalytic activity is lower than that of LMN1. Although the O adsorption peak is seen in the high resolution O1s spectrum presented in Fig. 9c, the absorption curve in Fig. 9a shows that LBM has the lowest oxygen vacancies. This is due to the fact that Ba substituted to La and Nd atoms does not have improved catalytic performance due to its low oxygen gap forming energy [48]. It is thought that the adsorption peak in the XPS spectrum may be caused by the OH and COOH groups attached to the surface after production or due to environmental effects. Enhanced oxygen vacancy generation energy is more favorable for oxygen reduction reactions. However, when sequential flame images are examined, it is seen that there are no atomization events due to the presence of particles such as transport to the flame region, micro-explosion. The only active phenomena during combustion are bubble ejection events. No significant effect on the combustion process was observed. $Nd_{0.7}Ba_{0.3}MnO_3$ NPs, on the other hand, have a surface area approximately twice as large (117.8164 m^2/s) compared to LBMs and are the NP with the largest oxygen vacancies after LMN1. The main problem here is that the NBM NPs cannot be sufficiently transported to the flame region due to their aggregation tendency. Sequential flame images show that most of the particle clusters are ejected out of the flame zone with micro-explosions towards the end of combustion.

The cation design in $La_{0.5}Nd_{0.3}Ba_{0.2}MnO_3$ perovskite type NPs provided the highest flame temperature of GA + LNBM1 fuel droplets loaded with these NPs. Although the flame temperature curve was similar to GA + LMB and GA + NBM for a while, the flame temperature suddenly increased to 407 °C after 225 °C, and the maximum flame temperature was measured as 469 °C. This maximum temperature is 274 °C higher than with pure fuel droplets. Because, during the combustion test, as seen in Fig. 22, after the flame temperature of 205 °C, it was observed that the flame temperature exceeded two times due to the burning of the NP agglemorates. The agglemorate formation of LNBM1 NPs is mainly due to their high molecular weight. This caused aggregation in the center of the droplet rather than particle aggregation on the surface. Therefore, it can be seen that less atomization phenomena occur compared to fuel droplets containing LM1, LNM1 and LBM. The micro-explosion at t = 1554 ms confirms this. Compared to other perovskite-type NPs, LNBM1 nanoparticles, which have more substituent elements and accordingly large surface area (393.4898 m^2/g), offer high catalytic activity. Although the absorption curve in Fig. 9a shows that it has a low oxygen vacancy, it is thought that the active oxygen in the lattice structure at the melt agglomerate temperature helps it exhibit high catalytic activity. In addition, when the O1s spectrum in Fig. 9d is examined, it can be seen that it has higher lattice oxygen compared to other particles.

3.6. Extinction times

Fig. 23 presents the extinction times of the fuel droplets. All particulate additives tended to prolong the extinction times of the gasoline droplet. The burning times of nanofuel droplets are characterized by bubble ejections, daughter droplets ejections, and micro-explosions that occur during combustion. However, unburned particle residues remaining on the wire towards the end of the combustion may also contribute to the prolongation of the combustion time.

GA + LNM1 fuel droplets were the fuel droplets that were depleted the latest. This is because the LNM1 NPs in these fuel droplets form an aggregate layer on the droplet surface. As the combustion continued, the fuel, which entered the vapor phase in the droplet, could not overcome the surface tension of this layer. As can be seen from the sequential flame images in Fig. 15, in the t = 1051–1203 ms range, GA + LNM1 fuel droplets swelled considerably due to the inability to expel the vapor phase from the droplet. The fuel droplet is relatively large compared to

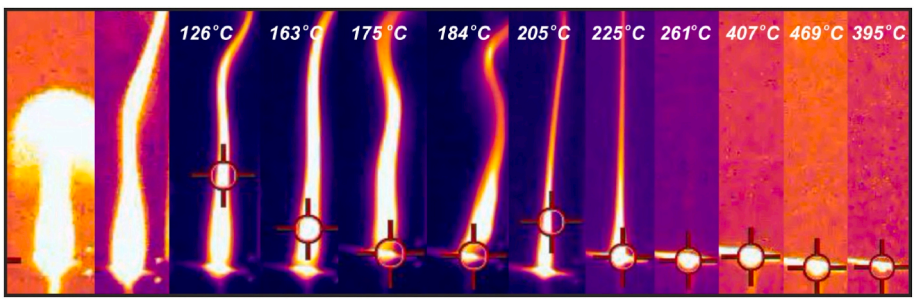


Fig. 22. Sequential thermal camera images of the GA + LNBM1 fuel droplet.

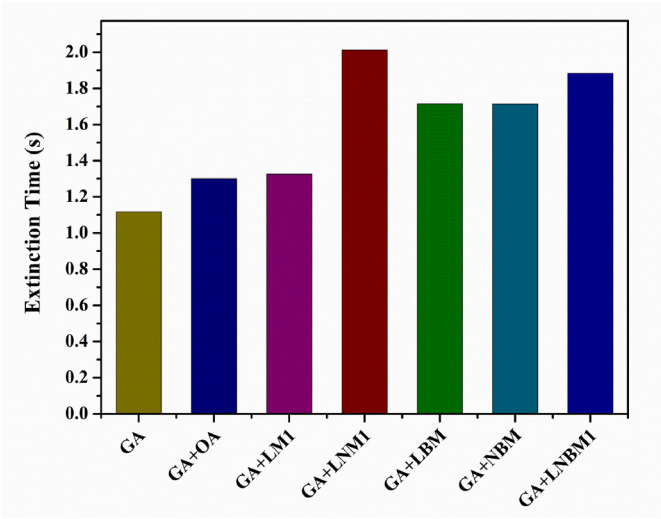


Fig. 23. Extinction times of NP-free and NP-doped fuel droplets.

other fuel droplets even towards the end of the combustion process, despite the severe atomization phenomena that occur around t = 1361 ms. This is because the vapor phase, which cannot be expelled from the droplet, puts the droplet into a cycle of swelling and contraction [45]. The fuel vapor was trapped in the droplet for some time and could not join the flame zone, resulting in a prolonged combustion time.

4. Conclusions

In this study, the combustion behavior of gasoline-based nanofuels containing 2.5 %wt. perovskite type NPs and 1 %wt. oleic acid surfactant at droplet scale was investigated. Characterization of NPs produced by the sol-gel technique was performed by SEM, XRD, XPS, BET and UV–Vis spectroscopy. The experiments were carried out under atmospheric conditions, under normal gravity and at room temperature.

- Characterization results showed that $LaMnO_3$ (LM1), $La_{0.7}Nd_{0.3}MnO_3$ (LNM1), $Nd_{0.7}Ba_{0.3}MnO_3$ (NBM), $La_{0.7}Ba_{0.3}MnO_3$ (LBM) and $La_{0.5}Nd_{0.3}Ba_{0.2}MnO_3$ (LNBM1) perovskite type nanoparticles were successfully produced with a particle diameter of 25–40 nm.
- Sequential flame images showed that the combustion process of nanofuels consisted of three stages; ignition (Stage 1), combustion with high kinetic energy droplet disruption phenomena (Stage 2), and combustion and diameter reduction (Stage 3) accompanied by low kinetic energy droplet disruption phenomena. It was observed that perovskite-type NPs at 2.5 %wt. Concentration plays an important role in the atomization of the gasoline droplet and the active disruption phenomena are daughter droplet formation, massive bubble ejection, and micro-explosion.
- Tests carried out on the droplet scale have shown that perovskite type NPs exhibit superior catalytic activity in the oxidation of soot and incompletely burned hydrocarbons formed as a result of gasoline combustion. It has been observed that the large surface area and high oxygen adsorption ability provided by perovskite-type NPs are responsible for this and that these properties can be further improved with the atoms substituted into their structures.
- All perovskite type NPs slightly increased the ignition delay of gasoline. The lowest increase was observed in the presence of LNM1 NPs and the highest ignition delay was observed in the presence of LNBM1 NPs.
- GA + LNM1 fuel droplets containing Nd-substituted $La_{0.7}Nd_{0.3}MnO_3$ NPs had the highest maximum flame temperature due to increasing soot oxidation at 245 °C. Ba substitutions contributed to the large surface formation with their high atomic diameters. However, varying amounts and positions in the catalyst design did not have a significant effect on the catalytic activity. The maximum flame temperature was measured as 469 °C in GA + LNBM1 fuel droplets containing $La_{0.5}Nd_{0.3}Ba_{0.2}MnO_3$ NPs with the largest surface area and lattice oxygen.
- The approach we developed for the production and design of new types of NPs customized for combustion in our study sheds light on the literature. In our future studies, the combustion behavior of these particles at high particle concentrations and their effects on engine and emission performance in an intermittent combustion test setup will be evaluated.

Declaration of competing interest

The authors declare that they have no known competing financial interests or personal relationships that could have appeared to influence the work reported in this paper.

Acknowledgments

The authors acknowledge the support of the Tarsus University Scientific Research Projects Coordination Department.

References

[1] R. Küçükosman, A.A. Yontar, K. Ocakoglu, Nanoparticle additive fuels: atomization, combustion and fuel characteristics, J. Anal. Appl. Pyrolysis 165 (2022), 105575, https://doi.org/10.1016/J.JAAP.2022.105575.
[2] L. Bao, W. Fu, F. Li, Y. Liu, H. Bi, C. Jiang, et al., Experiments on macroscopic spray characteristics of diesel-ethanol with dispersed cerium nanoparticles, J. Energy Inst. 93 (2020) 2186–2196, https://doi.org/10.1016/J.JOEI.2020.06.001.
[3] T. Kegl, A. Kovač Kralj, B. Kegl, M. Kegl, Nanomaterials as fuel additives in diesel engines: a review of current state, opportunities, and challenges, Prog. Energy Combust. Sci. 83 (2021), 100897, https://doi.org/10.1016/J.PECS.2020.100897.
[4] S.A. Patil, D.V. Shinde, D.Y. Ahn, D.V. Patil, K.K. Tehare, V.V. Jadhav, et al., A simple, room temperature, solid-state synthesis route for metal oxide nanostructures, J. Mater. Chem. A 2 (2014) 13519–13526, https://doi.org/10.1039/C4TA02267J.
[5] A.V. Nikam, B.L.V. Prasad, A.A. Kulkarni, Wet chemical synthesis of metal oxide nanoparticles: a review, CrystEngComm 20 (2018) 5091–5107, https://doi.org/10.1039/C8CE00487K.
[6] A.P. LaGrow, M.O. Besenhard, A. Hodzic, A. Sergides, L.K. Bogart, A. Gavriilidis, et al., Unravelling the growth mechanism of the co-precipitation of iron oxide nanoparticles with the aid of synchrotron X-Ray diffraction in solution, Nanoscale 11 (2019) 6620–6628, https://doi.org/10.1039/C9NR00531E.
[7] N.A. Fathy, Carbon nanotubes synthesis using carbonization of pretreated rice straw through chemical vapor deposition of camphor, RSC Adv. 7 (2017) 28535–28541, https://doi.org/10.1039/C7RA04882C.
[8] M.R. Abhilash, A. Gangadhar, J. Krishnegowda, M. Chikkamadaiah, S. Srikantaswamy, Hydrothermal synthesis, characterization and enhanced photocatalytic activity and toxicity studies of a rhombohedral Fe2O3 nanomaterial, RSC Adv. 9 (2019) 25158–25169, https://doi.org/10.1039/C9RA04978A.
[9] L. Dörner, C. Cancellieri, B. Rheingans, M. Walter, R. Kägi, P. Schmutz, et al., Cost-effective sol-gel synthesis of porous CuO nanoparticle aggregates with tunable specific surface area, Sci. Rep. 9 (2019 91 2019) 1–13, https://doi.org/10.1038/s41598-019-48020-8.
[10] Q.-L. Yan, F.-Q. Zhao, K.K. Kuo, X.-H. Zhang, S. Zeman, L.T. DeLuca, Catalytic effects of nano additives on decomposition and combustion of RDX-, HMX-, and AP-based energetic compositions, Prog. Energy Combust. Sci. 57 (2016) 75–136, https://doi.org/10.1016/j.pecs.2016.08.002.
[11] N.F. Atta, A. Galal, E.H. El-Ads, Perovskite nanomaterials – synthesis, characterization, and applications. Perovskite mater - synth characterisation, Prop Appl (2016), https://doi.org/10.5772/61280.
[12] D. Navas, S. Fuentes, A. Castro-Alvarez, E. Chavez-Angel, Review on sol-gel synthesis of perovskite and oxide nanomaterials, Gels 7 (2021) 275, https://doi.org/10.3390/GELS7040275, 2021;7:275.
[13] Q. Yang, G. Liu, Y. Liu, Perovskite-type oxides as the catalyst precursors for preparing supported metallic nanocatalysts: a review, Ind. Eng. Chem. Res. 57 (2017) 1–17, https://doi.org/10.1021/ACS.IECR.7B03251.
[14] P. Deng, P. Chen, H. Fang, R. Liu, X. Guo, The combustion behavior of boron particles by using molecular perovskite energetic materials as high-energy oxidants, Combust. Flame 241 (2022), https://doi.org/10.1016/j.combustflame.2022.112118.
[15] P. Ciambelli, S. Cimino, S. De Rossi, M. Faticanti, L. Lisi, G. Minelli, et al., AMnO3 (A=La, Nd, Sm) and Sm1−xSrxMnO3 perovskites as combustion catalysts: structural, redox and catalytic properties, Appl. Catal. B Environ. 24 (2000) 243–253, https://doi.org/10.1016/S0926-3373(99)00110-1.

[16] R. Spinicci, A. Delmastro, S. Ronchetti, A. Tofanari, Catalytic behaviour of stoichiometric and non-stoichiometric LaMnO3 perovskite towards methane combustion, Mater. Chem. Phys. 78 (2003) 393–399, https://doi.org/10.1016/S0254-0584(02)00218-3.
[17] C. Zhang, Y. Guo, Y. Guo, G. Lu, A. Boreave, L. Retailleau, et al., LaMnO3 perovskite oxides prepared by different methods for catalytic oxidation of toluene, Appl. Catal. B Environ. 148–149 (2014) 490–498, https://doi.org/10.1016/J.APCATB.2013.11.030.
[18] G. Koch, M. Hävecker, D. Teschner, S.J. Carey, Y. Wang, P. Kube, et al., Surface conditions that constrain alkane oxidation on perovskites, ACS Catal. 10 (2020) 7007–7020, https://doi.org/10.1021/ACSCATAL.0C01289/ASSET/IMAGES/LARGE/CS0C01289_0008.JPEG.
[19] C. Díaz, L. Urán, A. Santamaria, Preparation method effect of La0.9K0.1Co0.9Ni0.1O3 perovskite on catalytic soot oxidation, Fuel 295 (2021), 120605, https://doi.org/10.1016/J.FUEL.2021.120605.
[20] T. Ruh, R. Buchinger, L. Lindenthal, F. Schrenk, C. Rameshan, CO oxidation capabilities of La- and Nd-based perovskites, Fuel 3 (2022) 31–43, https://doi.org/10.3390/FUELS3010003, 2022;3:31–43.
[21] R. Küçükosman, A. Alper Yontar, C. Gökhan Ünlü, K. Ocakoglu, Combustion and secondary atomization behavior of nanofuel droplets laden with hematite, magnetite and lanthanum orthoferrites nanoparticles, Propellants, Explos. Pyrotech. (2023), e202300028, https://doi.org/10.1002/PREP.202300028.
[22] Y. Gan, L. Qiao, Radiation-enhanced evaporation of ethanol fuel containing suspended metal nanoparticles, Int. J. Heat Mass Tran. 55 (2012) 5777–5782, https://doi.org/10.1016/J.IJHEATMASSTRANSFER.2012.05.074.
[23] H. Dautzenberg, Polymeric stabilization of colloidal dispersions, in: Von Donald H. Napper. ISBN 0-12-513980-2. London/New York/etc.: Academic Press Inc. 1983. XVIII, 428 S., Lwd. Acta Polym, vol. 36, 1985, https://doi.org/10.1002/ACTP.1985.010360819, 457–457.
[24] A. Miglani, S. Basu, R. Kumar, Insight into instabilities in burning droplets, Phys. Fluids 26 (2014), 032101, https://doi.org/10.1063/1.4866866.
[25] Değirmenci H, Küçükosman R, Alper Yontar A. An experimental study on droplet-scale combustion and atomization behavior in pure ethanol, methanol, and trimethyl borate, and their blends. Fuel 2024;357:129716. https://doi.org/10.1016/J.FUEL.2023.129716.
[26] R. Küçükosman, A.A. Yontar, K. Ocakoglu, Experimental studies on combustion and atomization characteristics of aliphatic and aromatic hydrocarbons droplets, J. Energy Inst. 108 (2023), 101249, https://doi.org/10.1016/J.JOEI.2023.101249.
[27] R. Küçükosman, A.A. Yontar, C.G. Ünlü, K. Ocakoglu, Effects of Spinel Oxide Combustion Catalysts on the Combustion Behavior and Secondary Atomization Mechanism of Gasoline Droplets, 2023, https://doi.org/10.1080/00102202.2023.2228471.
[28] S.A. Hosseini, B. Mehri, A. Niaei, B. Izadkhah, C. Alvarez-Galvan, J.G.L. Fierro, Selective catalytic reduction of NOxby CO over LaMnO3nano perovskites prepared by microwave and ultrasound assisted sol–gel method, J. Sol. Gel Sci. Technol. 85 (2018) 647–656, https://doi.org/10.1007/S10971-017-4568-8/METRICS.
[29] Q. Liu, F. Wang, H. Lin, Y. Xie, N. Tong, J. Lin, et al., Surface oxygen vacancy and defect engineering of WO3 for improved visible light photocatalytic performance, Catal. Sci. Technol. 8 (2018) 4399–4406, https://doi.org/10.1039/C8CY00994E.
[30] T. Seiyama, Total Oxidation of Hydrocarbons on Perovskite Oxides 34 (2006) 281–300, https://doi.org/10.1080/01614949208016313.
[31] S. Chen, B. Pan, L. Zeng, S. Luo, X. Wang, W. Su, La2Sn2O7 enhanced photocatalytic CO2 reduction with H2O by deposition of Au co-catalyst, RSC Adv. 7 (2017) 14186–14191, https://doi.org/10.1039/C7RA00765E.
[32] B.M. Abu-Zied, A. Khan, Microwave-assisted synthesis of micro/nano NdO powders, J. Mater. Res. Technol. 9 (2020) 10478–10490, https://doi.org/10.1016/J.JMRT.2020.07.006.
[33] Y. Zhou, Y. Li, P. Han, Y. Dang, M. Zhu, Q. Li, et al., A novel low-dimensional heteroatom doped Nd2O3 nanostructure for enhanced electrochemical sensing of carbendazim, New J. Chem. 43 (2019) 14009–14019, https://doi.org/10.1039/C9NJ02778E.
[34] S. Chakrabarti, S. Ginnaram, S. Jana, Z.Y. Wu, K. Singh, A. Roy, et al., Negative voltage modulated multi-level resistive switching by using a Cr/BaTiOx/TiN structure and quantum conductance through evidence of H2O2 sensing mechanism, Sci. Rep. 7 (2017 71 2017) 1–13, https://doi.org/10.1038/s41598-017-05059-9.
[35] I.A. Ibadurrohman, N. Hamidi, L. Yuliati, The role of the unsaturation degree on the droplet combustion characteristics of fatty acid methyl ester, Alex. Eng. J. 61 (2022) 2046–2060, https://doi.org/10.1016/J.AEJ.2021.07.038.
[36] F. Liu, Y. Hua, H. Wu, C.F. Lee, Y. Li, Experimental investigation of polycyclic aromatic hydrocarbons growth characteristics of gasoline mixed with methanol, ethanol, or n-butanol in laminar diffusion flames, Energy Fuels 32 (2018) 6823–6833, https://doi.org/10.1021/ACS.ENERGYFUELS.8B00693.
[37] W. Merchan-Merchan, S. McCollam, J.F.C. Pugliese, Soot formation in diffusion oxygen-enhanced biodiesel flames, Fuel 156 (2015) 129–141, https://doi.org/10.1016/J.FUEL.2015.04.011.
[38] D.C.K. Rao, S. Karmakar, S. Basu, Atomization characteristics and instabilities in the combustion of multi-component fuel droplets with high volatility differential, Sci. Rep. 7 (2017 71 2017) 1–15, https://doi.org/10.1038/s41598-017-09663-7.
[39] A. Miglani, S. Basu, Effect of particle concentration on shape deformation and secondary atomization characteristics of a burning nanotitania dispersion droplet, J. Heat Tran. 137 (2015), https://doi.org/10.1115/1.4030394/383864.
[40] W. Shang, S. Yang, T. Xuan, Z. He, J. Cao, Experimental studies on combustion and microexplosion characteristics of N-alkane droplets, Energy Fuels 34 (2020) 16613–16623, https://doi.org/10.1021/ACS.ENERGYFUELS.0C02904.
[41] Y. Gan, L. Qiao, Combustion characteristics of fuel droplets with addition of nano and micron-sized aluminum particles, Combust. Flame 158 (2011) 354–368, https://doi.org/10.1016/J.COMBUSTFLAME.2010.09.005.
[42] C.K. Law, Internal boiling and superheating in vaporizing multicomponent droplets, AIChE J. 24 (1978) 626–632, https://doi.org/10.1002/AIC.690240410.
[43] I. Javed, S.W. Baek, K. Waheed, Autoignition and combustion characteristics of kerosene droplets with dilute concentrations of aluminum nanoparticles at elevated temperatures, Combust. Flame 162 (2015) 774–787, https://doi.org/10.1016/J.COMBUSTFLAME.2014.08.018.
[44] I. Javed, S.W. Baek, K. Waheed, Autoignition and combustion characteristics of heptane droplets with the addition of aluminium nanoparticles at elevated temperatures, Combust. Flame 162 (2015) 191–206, https://doi.org/10.1016/J.COMBUSTFLAME.2014.07.015.
[45] S. Basu, A. Miglani, Combustion and heat transfer characteristics of nanofluid fuel droplets: a short review, Int. J. Heat Mass Tran. 96 (2016) 482–503, https://doi.org/10.1016/J.IJHEATMASSTRANSFER.2016.01.053.
[46] S. Royer, D. Duprez, F. Can, X. Courtois, C. Batiot-Dupeyrat, S. Laassiri, et al., Perovskites as substitutes of noble metals for heterogeneous catalysis: dream or reality, Chem. Rev. 114 (2014) 10292–10368, https://doi.org/10.1021/CR500032A.
[47] Z. Li, M. Meng, Y. Zha, F. Dai, T. Hu, Y. Xie, et al., Highly efficient multifunctional dually-substituted perovskite catalysts La1−xKxCo1−yCuyO3−δ used for soot combustion, NOx storage and simultaneous NOx-soot removal, Appl. Catal. B Environ. (2012), https://doi.org/10.1016/J.APCATB.2012.03.022. Complete: 65–74.
[48] Q. Ji, L. Bi, J. Zhang, H. Cao, X.S. Zhao, The role of oxygen vacancies of ABO3 perovskite oxides in the oxygen reduction reaction, Energy Environ. Sci. 13 (2020) 1408–1428, https://doi.org/10.1039/D0EE00092B.
[49] D. Chen, C. Chen, Z.M. Baiyee, Z. Shao, F. Ciucci, Nonstoichiometric oxides as low-cost and highly-efficient oxygen reduction/evolution catalysts for low-temperature electrochemical devices, Chem. Rev. 115 (2015) 9869–9921, https://doi.org/10.1021/ACS.CHEMREV.5B00073.
[50] T. Hyodo, M. Hayashi, N. Miura, N. Yamazoe, Catalytic activities of rare-earth manganites for cathodic reduction of oxygen in alkaline solution, J. Electrochem. Soc. 143 (1996) L266–L267, https://doi.org/10.1149/1.1837229/XML.
[51] J. Zhang, Z. Xia, L. Dai, Carbon-based electrocatalysts for advanced energy conversion and storage, Sci. Adv. 1 (2015), https://doi.org/10.1126/SCIADV.1500564/ASSET/1345A626-3DFC-4D7F-B0FA-0EA2E2EEE073/ASSETS/GRAPHIC/1500564-F11.JPEG.
[52] J. Suntivich, H.A. Gasteiger, N. Yabuuchi, H. Nakanishi, J.B. Goodenough, Y. Shao-Horn, Design principles for oxygen-reduction activity on perovskite oxide catalysts for fuel cells and metal-air batteries, Nat. Chem. 3 (2011) 546–550, https://doi.org/10.1038/NCHEM.1069.
[53] Z. Sihaib, F. Puleo, G. Pantaleo, V. La Parola, J.L. Valverde, S. Gil, et al., The effect of citric acid concentration on the properties of LaMnO3 as a catalyst for hydrocarbon oxidation, Catalyst 9 (2019), https://doi.org/10.3390/CATAL9030226, 226 2019;9:226.
[54] F. Papa, L. Patron, O. Carp, C. Paraschiv, B. Ioan, Catalytic activity of neodymium substituted zinc ferrites for oxidative conversion of methane, J. Mol. Catal. Chem. 299 (2009) 93–97, https://doi.org/10.1016/J.MOLCATA.2008.10.036.